NANO · MICRO small
www.small-journal.com

Sol-Gel-Derived Ordered Mesoporous High Entropy Spinel Ferrites and Assessment of Their Photoelectrochemical and Electrocatalytic Water Splitting Performance

Marcus Einert, Arslan Waheed, Stefan Lauterbach, Maximilian Mellin, Marcus Rohnke, Lysander Q. Wagner, Julia Gallenberger, Chuanmu Tian, Bernd M. Smarsly, Wolfram Jaegermann, Franziska Hess, Helmut Schlaad, and Jan P. Hofmann**

The novel material class of high entropy oxides with their unique and unexpected physicochemical properties is a candidate for energy applications. Herein, it is reported for the first time about the physico- and (photo-) electrochemical properties of ordered mesoporous (CoNiCuZnMg)Fe_2O_4 thin films synthesized by a soft-templating and dip-coating approach. The A-site high entropy ferrites (HEF) are composed of periodically ordered mesopores building a highly accessible inorganic nanoarchitecture with large specific surface areas. The mesoporous spinel HEF thin films are found to be phase-pure and crack-free on the meso- and macroscale. The formation of the spinel structure hosting six distinct cations is verified by X-ray-based characterization techniques. Photoelectron spectroscopy gives insight into the chemical state of the implemented transition metals supporting the structural characterization data. Applied as photoanode for photoelectrochemical water splitting, the HEFs are photostable over several hours but show only low photoconductivity owing to fast surface recombination, as evidenced by intensity-modulated photocurrent spectroscopy. When applied as oxygen evolution reaction electrocatalyst, the HEF thin films possess overpotentials of 420 mV at 10 mA cm^{-2} in 1 M KOH. The results imply that the increase of the compositional disorder enhances the electronic transport properties, which are beneficial for both energy applications.

1. Introduction

High entropy materials have attracted great attention in the materials science community due to the exploration of novel and unexpected physicochemical properties.[1] The concept of entropically stabilized crystal structures based on the incorporation of five or more cations in equiatomic concentrations at a single crystallographic site, leads to an increase of the configurational entropy (S_{config}). This, in turn, results in an entropic stabilization effect in regard to the reaction of formation, since the free Gibbs reaction enthalpy contains a significant negative contribution $T\Delta S_{mix}$ of the mixing, compared to the single pure compounds, which overall dominates the enthalpy according to the general Gibbs equation $\Delta G = \Delta H - T\Delta S$.[2] The principal concept of high entropy alloys was extended to high entropy oxides (HEO), sulfides, fluorites, and carbides in recent years.[3–7] Up to date, high entropy

---

M. Einert, A. Waheed, M. Mellin, J. Gallenberger, C. Tian, W. Jaegermann, J. P. Hofmann
Surface Science Laboratory
Department of Materials and Earth Sciences
Technical University of Darmstadt
Otto-Berndt-Strasse 3 64287, Darmstadt, Germany
E-mail: marcuseinert@gmx.de; hofmann@surface.tu-darmstadt.de

S. Lauterbach
Institute for Applied Geosciences
Geomaterial Science
Technical University of Darmstadt
Schnittspahnstrasse 9 64287, Darmstadt, Germany

The ORCID identification number(s) for the author(s) of this article can be found under https://doi.org/10.1002/smll.202205412.

DOI: 10.1002/smll.202205412

M. Rohnke, L. Q. Wagner, B. M. Smarsly
Center for Materials Research
Justus Liebig University Giessen
Heinrich-Buff-Ring 17 35392, Giessen, Germany

L. Q. Wagner, B. M. Smarsly
Institute for Physical Chemistry
Justus-Liebig University
Heinrich-Buff-Ring 17 35392, Giessen, Germany

F. Hess
Institute of Chemistry
Technical University Berlin
Strasse des 17. Juni 124 10623, Berlin, Germany

H. Schlaad
University of Potsdam
Institute of Chemistry
Karl-Liebknecht-Str. 24–25 14476, Potsdam, Germany

oxides have been demonstrated as a promising material class, since unique and tailored material properties can be designed, such as unusually high dielectric constants,[8] enhanced and stable lithium ion transport and storage properties,[9] and exceptional (electro-) catalytic activities.[10,11] These remarkable and unprecedented performances have been generally ascribed to the numerous possible interactions (synergistic effects) of the constituting elements, which will modify the corresponding electronic structure and may induce charge carrier transfer among the crystallographic sites,[12] and thus, enables a wide range of novel applications of high entropy oxides with tailored (electronic) properties.[13]

Especially the design of HEOs on the nanoscale by sol-gel reactions is highly challenging, since the hydrolysis and condensation reactions have to be controlled precisely upon the synthesis in order to obtain a defined structure on two length scales, the peculiar crystalline structure with a statistical occupancy and, at the same time, the desired nanostructures. Besides, synthesis parameters have to be chosen carefully in order to avoid the formation of precipitates in the starting solution or phase separation within the alloy structure. Up to now, predominantly preparation methods for solid-state HEOs are reported, which usually result in micron-sized materials.[14,15] However, the design of nanosized HEOs is highly indicated since the mass transport and surface reactivity can potentially be strongly enhanced for nanomaterials due to the increase of surface area and the creation of short diffusion paths in the pore space and/or the solid nanostructured phase. Polymer templating of inorganic structures is a facile synthetic way to produce such desired nanomaterials with a high content of porosity. Since Brinker and others established the evaporation-induced self-assembly (EISA) process in the early 1990's,[16] numerous metal oxide systems have been prepared as mesoporous thin films by the soft-templating approach.[17–21] However, the majority of commercially available block copolymers, such as from the Pluronic family, result in a breakdown of the mesoporous network upon annealing.[22] This collapse of the mesopore framework is due to the formation of insufficiently thick pore walls which are unable to withstand nucleation and growth of nanometer-sized crystalline domains, which are typically larger than 5 nm in dimension.[19,23,24] The diblock copolymer KLE (i.e., poly(ethylene-*co*-butylene)-*block*-poly(ethylene oxide), KL stands for Kraton Liquid and E for poly(ethylene oxide)), however, has revealed superior templating properties, due to its high thermal stability (up to 400 °C) and high hydrophilic-hydrophobic contrast enabling the development and growth of thick pore walls within the inorganic network.[17,18,25,26] Therefore, the amorphous framework can be transformed directly into the corresponding crystalline phase with retention of the mesopore periodicity. Due to its unique properties, KLE has been utilized as suitable template for the direct synthesis of various large-mesoporous metal oxide films—among others ferrites—with nanocrystalline walls and repeat distances typically ranging from 15 nm to 20 nm most frequently reported by the Brezesinski group.[17–19,21,24,27,28] Furthermore, the synthesis of numerous highly ordered ferrites (XFe_2O_4 with X = Co, Cu, Mg, Ni, Zn, Cd) were successfully prepared by the same group utilizing the EISA process.[20,28–30]

Nanostructuring of photoelectrodes for photoelectrochemical (PEC) water splitting has been broadly utilized as a conceptual synthetic approach to address two main drawbacks of certain metal oxides, which are their limitation in photovoltage and short charge carrier diffusion lengths.[31–34] The decrease of the lateral extensions of the migration paths results in the inhibition of bulk charge carrier recombination processes, as it has been reported for various metal oxide-based and nanostructured photoabsorbers, such as TiO_2,[35,36] α-Fe_2O_3,[37] WO_3,[38] $BiVO_4$,[39] CuO,[40] and ZnO.[41] Particularly ferrites are promising candidates as absorber materials for photoelectrodes due to their excellent absorption behavior in the visible spectrum of light, earth abundancy, chemical stability in aqueous media, and nontoxicity.[42] A broad spectrum of iron-based oxides have already been investigated for solar water splitting and their photoelectrochemical properties and the future perspectives are described in detail in literature.[43–47] Spinel ferrites, such as $ZnFe_2O_4$,[22] $CuFe_2O_4$,[48] $MgFe_2O_4$,[49] and $CaFe_2O_4$[50] have been stated to be photoactive materials showing the best reported cathodic photocurrent density of –1.82 mA cm^{-2} at 0.4 V versus reversible hydrogen electrode (RHE). Compared to theoretical calculations of p-type $CuFe_2O_4$, a maximum photocurrent density of ≈27 mA cm^{-2} which corresponds to solar-to-hydrogen conversion efficiency of ≈33% can be achieved in alkaline media.[48] Hence, ferrite-based photoelectrodes still suffer under overall poor PEC performance owing to low photocurrents and -voltages. Additionally, photodegradation is a commonly observed phenomenon in metal oxides when the oxidation potential and reduction potential—from an energetically point of view—above the valence band maximum (VBM, or hole polaron formation energy, n-type) and below the conduction band minimum (CBM, or electron polaron formation energy, p-type) since photogenerated electron-hole pairs are capable of oxidizing and reducing the semiconductor itself. In essence, self-oxidation and -reduction are competitive reaction pathways with respect to the desired water splitting reaction and materials design strategies, among others, nanostructuring and morphology control, might help in the context of efficient charge carrier separation since short diffusion paths to reaction sites are provided.[51]

Beside the utilization of spinel ferrites as photoelectrodes for solar water splitting, this material class has also been proven to efficiently catalyze the oxygen evolution reaction (OER), which is known to be the kinetic bottleneck for electrocatalytic water splitting due to its mechanistic complexity.[12,52] The main drawback of state-of-the-art OER catalysts, such as IrO_2 and RuO_2, are their high-cost and scarcity. Consequently, exploration of novel low-cost catalysts to make them economically attractive is indicated. In principle, the electronic conductivity and band structure of the catalyst surface predominantly determines the OER performance of transition metal (TM) oxides.[53] For spinel structured metal oxides, especially the octahedral sites have been identified as the catalytically active centers for the OER.[54] Among metal oxides crystallizing in the spinel phase, core-ring structured $NiCo_2O_4$ nanoplatelets showed with 315 mV at 100 mA cm^{-2} one of the highest OER activities in alkaline solution.[55] Spinel ferrites, such as $CoFe_2O_4$,[56] $NiFe_2O_4$,[57] and $CuFe_2O_4$[58] have also demonstrated to be efficient electrocatalysts showing overpotentials between 287 mV to 520 mV at 10 mA cm^{-2} in 1 M KOH. The yet low OER performance of ferrites was improved through partial substitution of the Fe^{3+} by Ni and Mn forming $CoFe_{2-x}M_xO_4$ (M = Ni, Mn) materials[52] or the preparation of nanoparticular (3–6 nm) $Co_xNi_{1-x}Fe_2O_4$ electrocatalysts,[59] both methods being a promising synthetic strategy for increasing the catalytic activity by substitution effects. However, further optimization in terms of cationic substituting affects needs to be accomplished in order to elucidate the maximum OER activity of ferrites. In general, the substitution of (transition metal) cations within the spinel structure significantly affects the electronic structure, which in turn dominates the electrocatalytic properties through manipulation of the adsorption energy of reaction intermediates. In particular, the formation of multi-metallic oxides rather than single-metal catalysts is beneficial in terms of inter-atomic charge transfer, which occurs via a hopping process, because charge transfer between cations with corresponding isoenergetic electron states require low activation energies.[58,60] Hence, mixed-valence oxides can be tailored in order to tune the electronic structure and thus to improve intrinsic properties, such as the conductivity and catalytic performance substantially.[61] The implementation of multiple elements within a compound results in a perturbation of the electronic structure, which is described in literature as ligand effect.[12,62–64] Additionally, the incorporation of cations with distinct ionic radii will unavoidably induce structural defects within the crystallographic order coming along with changes in lattice parameters, in turn, affecting the superposition of atomic orbitals, and therefore also the electronic structure.[12] Structural defects may impact the catalytic activity tremendously, for example, by creation of energetically favorized adsorption sites, such as oxygen vacancies, the descriptor of the lattice oxygen mechanism (LOM), prevalent under alkaline OER conditions.[65] Spinel-structured HEOs represent such multi-metallic systems with beneficial properties for the OER making them an attractive candidate for low-cost catalysts.[1] Entropy-induced structure stabilization is also reported to be the reason for improved OER stability in comparison to binary and ternary materials possessing—at the same time—equal overpotentials.[15,66] Stenzel et al. identified an optimized elemental composition for spinel-structured HEOs resulting in low overpotentials of 293 mV (at 10 mA cm^{-2}).[66] With respect to HEOs, photocatalytic hydrogen production,[67] photoelectrochemical water reduction[23] and oxidation[68] have rarely been studied, showing up to date only low to moderate photocurrents and hydrogen evolution efficiencies. A recent study of our group on (non-ordered) mesoporous spinel HEO revealed a low photoresponse under visible light irradiation, most likely owing to structural defects induced by implementation of several cations with distinct radii.[23] However, the same HEO showed good electrocatalytic activities with overpotentials of 350 mV at 10 mA cm^{-2}.[23] A certain form of HEOs, namely high entropy ferrites (HEF), have recently been investigated as high-performing sulfur host material in lithium-sulfur batteries,[69] as microwave absorbing material,[70,71] magnetic insulator,[72] and oxygen evolution catalyst.[73] Pan and Lu et al. studied the catalytic oxygen evolution on $Co_{0.2}Ni_{0.2}Cu_{0.2}Zn_{0.2}Fe_{0.2}Fe_2O_4$ and found that the disordered occupation of multivalent cations increases the configurational entropy, which facilitates the formation of structurally stable oxygen vacancies.

Since the $(CoNiCuZnMg)Fe_2O_4$ system is already proven to form highly robust entropically stabilized structures with notable properties[69] and the surface area were demonstrated to enhance the catalytic activity of HEOs significantly,[23] we chose an ordered mesoporous HEF thin film—offering plenty of reaction sites—as model catalyst for assessment of the (photo-) electrocatalytic performance. The main goal of the present work is to study the fundamental impact of a nanoscale framework on the electrocatalytic and photoelectrochemical water splitting properties of mesoporous HEF thin films and to elucidate how the compositional disorder on a single crystallographic site affects both the surface morphology and electronic band structure. By variation of the calcination time, the morphology and crystallinity of the high entropy materials were modified on the nanoscale. These tailored manipulations of the nanostructure allowed us to resolve the link between enhanced electronic transport properties and OER activity of ordered mesoporous HEF electrodes.

2. Results and Discussion

2.1. Structural and Morphological Characterization

In order to attain periodically ordered HEF nanostructures, the synthesis parameters were optimized systematically. The ordered mesoporous high entropy oxides were prepared utilizing KLE (molar mass 7.8 kg mol^{-1}, 42 wt% ethylene oxide) as templating polymer and metal nitrates as inorganic precursors both carefully selected building blocks which can be homogenously dissolved in polar solvents.[17] All components were dissolved in a mixture of ethanol and 2-methoxyethanol, and thin films were prepared by dip-coating making use of the evaporation-induced self-assembly (EISA) process.[16] Especially the usage of 2-methoxyethanol as co-solvent is beneficial in terms of controlling the evaporation rate of the dip-coating solution upon the EISA process,[74] wherefore the optimum ratio of both solvents needed to be elucidated. Hydrolysis and condensation reactions (classic sol-gel chemistry) of the inorganic precursors produce an oxide-bridged amorphous metal ion network in coexistence with spherical KLE micelles upon evaporation of the organic solvent in a defined humidity-controlled atmosphere (**Scheme 1**). Optimized heating conditions included a pre-stabilization step at 260 °C for 15 h, a pre-conditioning which enhances the condensation reactions of the hybrid network and a commonly applied (stabilization) step for the successful transformation of the hybrid (organic/inorganic) structure into an ordered mesoporous metal oxide.[27,75] As the impact of the final annealing time on the electrocatalytic and photoelectrochemical properties was investigated in the underlying study, the control parameters were chosen to be 10 min and 2 h for a calcination temperature of 600 °C in air. At this temperature, typically the crystallization of the initial hybrid network and the thermal degradation of the KLE template are induced. Owing to the favorable templating properties of KLE, sufficiently thick pore walls allow the uniform crystallization of nanocrystals under preservation of the mesopore framework upon heating. Accordingly, the amorphous composition can be transformed into a highly crystalline mesoporous thin film, while retaining the nanoscale periodicity.[18,19] This soft-templating method, also described as nanocasting approach,[76] allows the creation of ordered three-dimensional mesoporous architecture potentially offering a large number of reactive surface sites. The overall formation process of the mesoporous HEF thin films is illustrated schematically in Scheme 1.

Before discussing the effect of calcination time on the surface morphology, the influence of the configurational disorder

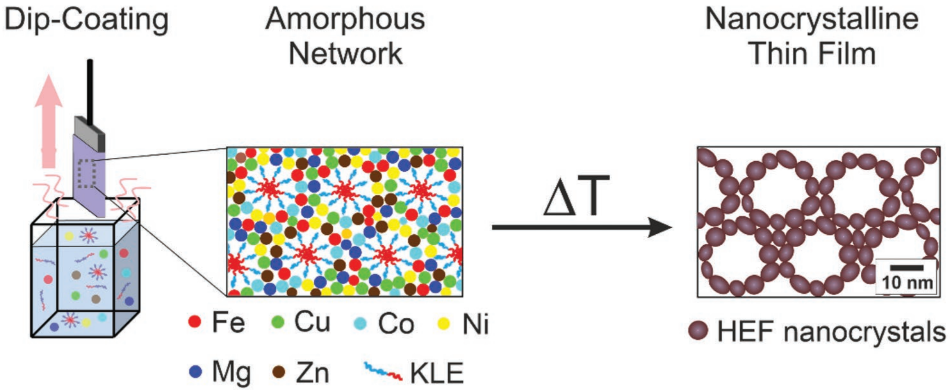

Scheme 1. Schematic drawing of the applied dip-coating process representing the formation of an amorphous network composed of six distinct cations, which is transformed into a nanocrystalline mesoporous framework after annealing.

on the surface topography was studied by comparison of the surface morphology of $CoNiCuZnFe_2O_4$ (incorporation of four distinct cations on one crystallographic site, later referred to as A-site medium entropy ferrite (MEF)) and $CoNiCuZnMgFe_2O_4$ (incorporation of five distinct cations on one crystallographic site, later referred to as A-site high entropy ferrite (HEF)) prepared both under the very same conditions (see Experimental part). Scanning electron microscopy (SEM) images of the MEF and HEF thin films after calcination at 600 °C for 10 min are shown in **Figure 1**A,B, respectively.

Both samples show spherical mesopores measuring 15–20 nm in size, which are arranged in a hexagonal arrangement. Interestingly, mesopore formation, more precisely the pore wall construction on the nanoscale, is moderately affected by implementing an additional element (magnesium) into the crystal structure of the ferrites. The addition of magnesium seems slightly to affect the surface morphology through development of less spherically shaped pores (Figure 1B). Importantly, for both MEF and HEF thin films, the long-range periodicity as well as the connectivity of pore walls—which are vital with respect to electrical conductivity[77]—are still structurally intact and were retained after calcination. All thin films were presented to be crack-free not only on the mesoscopic, but also on the macroscopic scale (see Figure S1, Supporting Information for large-area SEM images). The surface morphology of the calcined samples with an ordered arrangement of mesopores was additionally visualized by atomic force microscopy (AFM) (see Figure S2, Supporting Information) revealing the topography of the thin film surface with a typical root-mean-square roughness of 0.7 nm for KLE templated metal oxides (analyzed within an area of 500×500 nm^2). These soft-templated materials are, to the best of our knowledge, the first report on the synthesis of highly ordered, mesoporous and nanocrystalline high entropy assisted oxide thin films. Recently, the group of Brezesinski has reported on mesoporous multimetallic ferrite films, however incorporating fewer types of cations (and focusing solely on magnetic properties).[78] It is important to note that the precise control of hydrolysis and condensation reactions of six distinct metal precursors in the presence of the organic polymer (known to interact via hydrogen bridge linkage)[79] during the EISA process is a delicate task, which needs to be tailored in terms of precursor concentrations (affecting the reaction kinetics of the sol-gel reactions), the ratio of the used organic solvents (determining the evaporation rate of the solvent and thus the self-organization of the precursors), and the humidity in the dip-coating chamber (was chosen to be between 10 and 18%) also impacting the reaction kinetics and the overall formation of the condensed metal-oxide network.

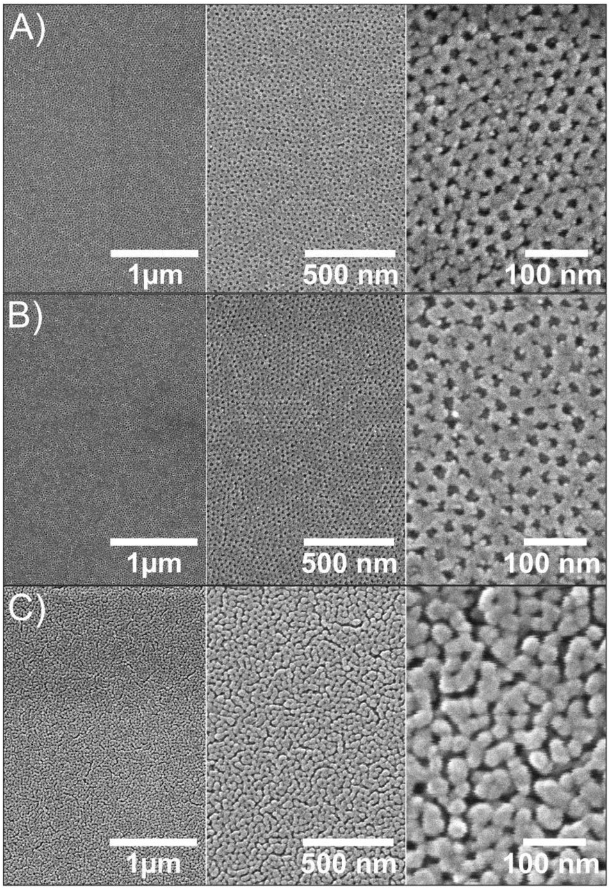

Figure 1. SEM images of mesoporous A) $CoNiCuZnFe_2O_4$ (MEF) and B) $CoNiCuZnMgFe_2O_4$ (HEF) thin films both stabilized for 12 h at 250 °C and calcined at 600 °C for 10 min and C) HEF thin film calcined at 600 °C for 2 h.

Since the porosity in sol-gel derived mesoporous TiO_2 thin films was found to be a function of calcination temperature and time,[80] the impact of annealing time on the morphological formation of the mesoporous HEF framework was analyzed. Therefore, the samples were calcined at 600 °C for 10 min (HEF-10 min) and 2 h (HEF-2 h) and systematically compared with each other. The SEM images in Figure 1 reveal different surface morphologies depending on calcination time. A thermally induced crystallite growth was initiated within the pore walls, resulting in elongated nanocrystals, upon prolonging the calcination time from 10 min (Figure 1B) to 2 h (Figure 1C). However, the in-plane pore morphology was well preserved even after a calcination time of 2 h. The findings are in good agreement with the temperature study on KLE-templated Bi_2O_3 nanostructures showing a comparable development of the thin film morphology upon increased annealing temperatures.[74]

For proving the existence of a highly entropic atomic configuration on the nanoscale, scanning transmission electron microscopy (STEM) combined with energy dispersive X-ray spectroscopy (EDS) was accomplished. **Figure 2**A,C show dark field STEM images and the elemental mappings of the corresponding nanocrystals for the HEF-10 min and HEF-2 h thin films, respectively. The EDS mappings confirm the presence of iron (red), cobalt (turquoise), nickel (yellow), copper (green), zinc (brown), and magnesium (blue), which are homogenously distributed within the high entropy nanostructures. Especially, for the HEF-10 min sample the pore walls are solely composed of the six metals and oxygen, as demonstrated in Figure 2A, initially added to the dip-coating solution in form of their nitrates. Figure 2B,D depicts the HRTEM images of HEF-10 min and HEF-2 h samples, respectively. Insets are added for iFFT filtered areas and selected area electron diffraction (SAED) patterns taken from larger areas of the same samples. The iFFT insets show the expected lattice spacing for the {220} set of planes in the cubic spinel structure with $a_0 = 8.39 \pm 0.1$ Å, and the SAED patterns also could consistently be indexed using this value.

The relative atomic concentrations of the inserted metals within the bulk structure were characterized by SEM based EDS. The atomic concentration for the HEF material were identified to be of 1.26 (standard deviation, SD 0.34): 1.03 (SD 0.25) : 0.96 (SD 0.32) : 1.05 (SD 0.46) : 1.1 (SD 0.59) : 8.53 (SD 0.79) for Mg:Co:Ni:Cu:Zn:Fe corresponding to the chemical formula $Co_{0.20}Ni_{0.19}Cu_{0.20}Zn_{0.21}Mg_{0.24}Fe_{1.65}O_{3.53}$. For the MEF samples, the atomic concentrations were determined to be 0.71 (SD 0.33): 0.74 (SD 0.34): 0.71 (SD 0.38): 0.71 (SD 0.61): 4.86 (SD 0.70) which represents the chemical formula $Co_{0.25}Ni_{0.24}Cu_{0.25}Zn_{0.25}Fe_{1.71}O_{3.56}$ (analyzed at and averaged from 17 distinct spots, normalized to Co, see Table S1, Supporting Information). Note that the theoretical calculations for the atomic ratio according to the chemical formula MFe_2O_4 (with M = Mg, Co, Ni, Cu, Zn and assuming that iron solely occupies B-sites corresponding to a normal spinel configuration) would be Mg:Co:Ni:Cu:Zn:Fe = 1 : 1 : 1 : 1 : 1 : 10 for the HEF samples. Therefore, Mg is evidently present overstoichiometrically, whereas Fe is found to be slightly understoichiometrically in concentration. Consequently, the determined molar fractions deviate up to 10% for

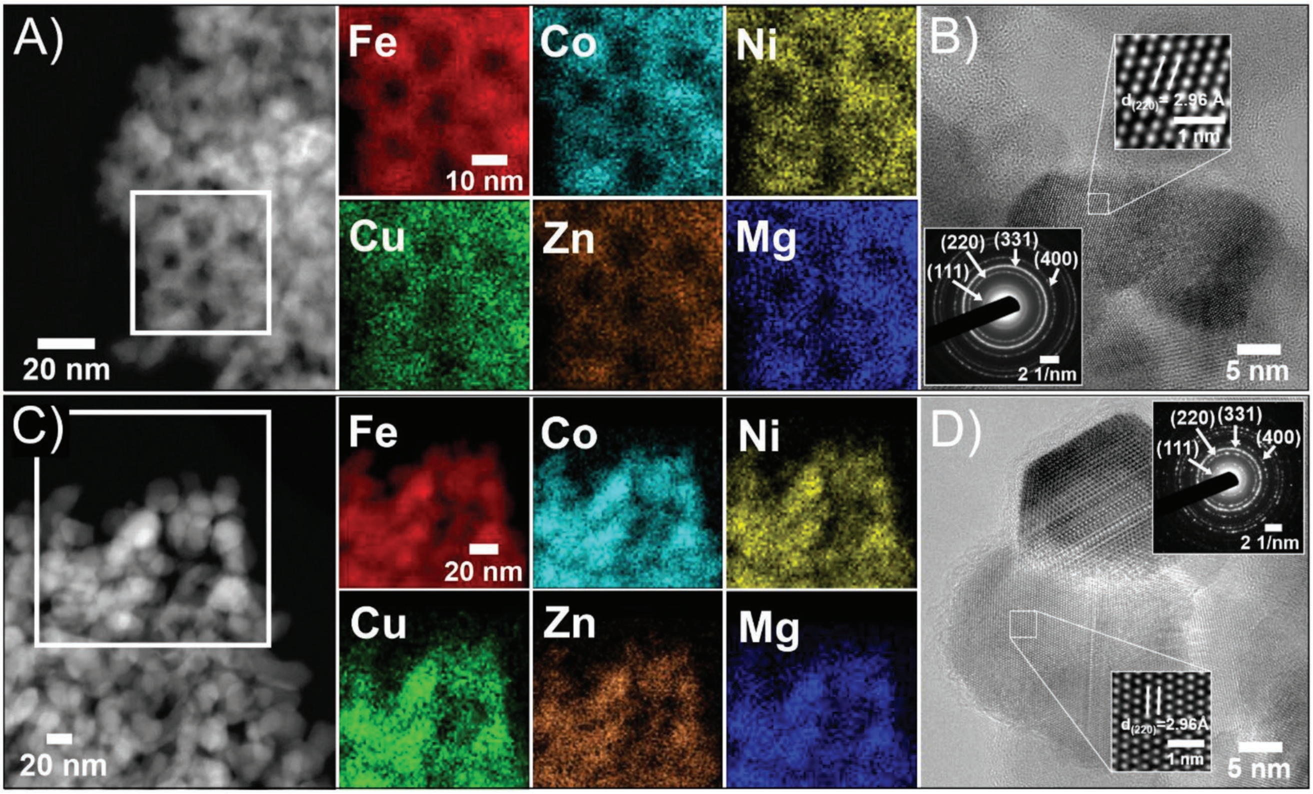

Figure 2. STEM dark field pictures and the corresponding EDS-based elemental mapping of iron (red), Co (turquoise), Ni (yellow), Cu (green), Zn (brown), and Mg (blue) for A) 10 min and C) 2 h at 600 °C calcined mesoporous HEF thin films. HR-TEM images of mesoporous HEF thin films prepared at 600 °C and held for B) 10 min and D) 2 h. Insets showing iFFT filtered images of the HRTEM images illustrating the lattice plane spacing of d_{220} of the spinel ferrite structure. SAED patterns from bulk areas including several crystallites were indexed for the cubic spinel phase.

Co, Ni, Cu, and Zn and 25% for Mg from the ideal stoichiometric value of 0.2 mol for the A-cations. However, this deviation—except for Mg—can be interpreted to be within the experimental error of the EDS analysis (estimated to be ±10%). The evaluation of the bulk concentration of the metals within HEF thin films is in agreement with the (theoretical) expected composition for the spinel phase. Furthermore, we have to highlight that the underlying materials are nanostructured and solution processed (sol-gel derived) materials, wherefore statistical deviations in the cation distribution are known be present.[28] Statistical thermodynamics (Boltzmann's entropy equation) allow the calculation of the configurational entropy, S_{config}, on a single crystallographic site of a multicomponent near-equiatomic system according to Equation (S1), Supporting Information.[81,82] ΔS_{config} equals 1.63 R and 1.38 R for the HEF and MEF samples, respectively (detailed calculation can be found in the Supporting Information). Based on the empirical classification by Murty et al.[81] describing "high-entropy" stabilized materials as compounds with $S_{config} \geq 1.5$ R, the phase formation of the underlying multicomponent ferrites can be considered accordingly to high entropy and medium entropy assisted structures. The spinels are structurally stabilized by the compositional disorder on the A-site. Since iron is known to occupy both A- and B-sites in spinels, EDS analysis do not allow at this stage a precise quantification and differentiation of the iron content on the respective crystallographic sites. Perspective work will focus on synchrotron-based characterization to determine the coordination sites of the cations quantitatively. The data acquired by STEM- and SEM-EDS are further supported by grazing-incidence wide-angle X-ray scattering (GIWAXS) measurements as presented in **Figure 3**A. The diffraction pattern of HEF-10 min (red) and HEF-2 h (blue) depicts Bragg signals, which can be assigned to the crystallographic structure of the cubic spinel phase with the space group symmetry $Fd\overline{3}m$ (space group No. 227). Via the Scherrer equation (applied for the (311)-peak) the average crystallite sizes of the materials were determined to be 7 nm for HEF-10 min and 10 nm for HEF-2 h HEF thin films. Due to the prolonged calcination time, a thermally induced crystal growth occurred (see above), which is also visualized in the TEM images in Figure 2. The lattice parameter, *a*, of the cubic spinel structure, which was calculated via the Bragg equation, was found to be 8.39 Å and 8.42 Å for the HEF-10 min and HEF-2 h samples, respectively. The lattice spacing of the unit cell, d_{111}, was found to be 4.843 Å for HEF-10 min and 4.862 Å for HEF-2 h. All parameters match well with the data for the cubic spinel phase and are also consistent with the lattice spacings observed by HR-TEM analysis (see insets Figure 2B,D) within the experimental and instrumental errors of ±0.1 Å, and for structural and chemical related, sol-gel derived HEO thin films.[23,83] Exclusively the spinel phase was observed by GIXRD and SAED. A closer inspection of the diffractogram (Figure S1) reveals a preferred orientation of the (511) lattice plane. This pronounced crystallographic (uniaxial) orientation relative to the plane of the substrate was already observed for KLE-templated Ta_2O_5.[84] The anisotropy of the diffraction patterns was explained by the presence of carbonaceous layers which facilitate oriented crystallographic alignment, wherefore the crystallization behavior was referred to "soft epitaxy", a mechanism, which is distinct from classical liquid phase epitaxy. Raman spectroscopy was supportively accomplished since conventional X-ray scattering methods are known to be less sensitive to poorly crystalline materials and small concentrations of secondary phases.[28] In agreement with literature (reporting about the same composition of HEF materials

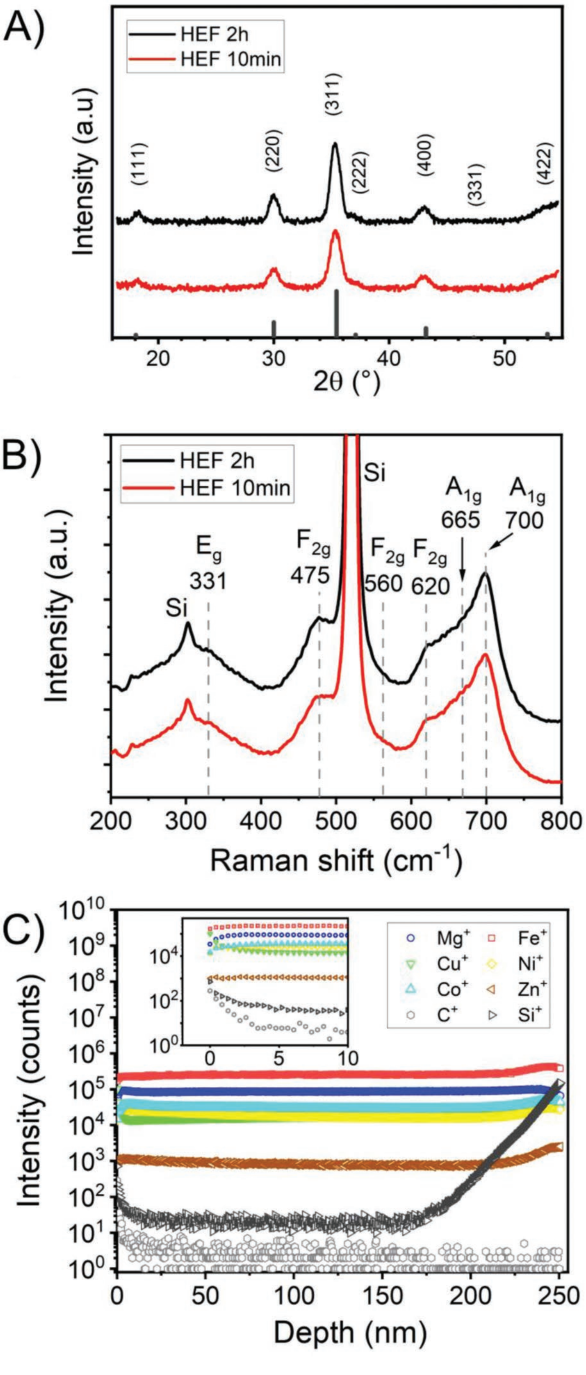

Figure 3. A) GIWAXS patterns of the HEF samples annealed at 600 °C for 10 min (red) and 2 h (blue). The line patterns (grey) represent the diffraction signals for cubic spinel phase ($Fd\overline{3}m$). B) Raman spectra of the HEF-10 min and HEF-2 h samples attained on a (100)-silicon substrate. C) ToF-SIMS depth profile of the HEF thin film. The film surface can be found at a depth of 0 nm. The interface to the substrate is at 250 nm.

for magnetic applications)[72] and according to group theory, six Raman-active phonon modes were detected in the wavenumber range between 200 cm^{-1} and 800 cm^{-1} (Figure 3B). The Raman spectrum in Figure 3B shows vibrational modes at 331 (E_g), 475 (F_{2g}), 560 (F_{2g}), 620 (F_{2g}), 665 (A_{1g}), and 670 (A_{1g}) cm^{-1}, also observed for single crystalline bulk $MgFe_2O_4$[85] and $ZnFe_2O_4$.[86,87] The peaks at 303 cm^{-1} and 520 cm^{-1} can be attributed to the (100) silicon substrate, being typically present in mesostructured materials deposited on silicon substrates.[30] The HEF-10 min and HEF-2 h samples shows no significant difference in the position of the appearing Raman-modes, demonstrating that both samples crystallize in a single-phase spinel structure and no phase transition occurs upon calcination. The presence of all phonon-modes is in accordance with other studies on ordered mesoporous ferrite thin films and representative for an partially inverse spinel configuration.[28,30,87] Conclusively, the Raman analysis support the outcome of the preceding structural characterization data proving the formation of phase-pure spinels. Besides, the Raman spectroscopy (highly sensitive to impurities) verifies that no side phases, such as hematite—an exceptional stable modification at such high temperatures—have been formed, which in turn further supports the assumption that the formation of the ferrites is entropically stabilized. The peak broadening of the Raman bands, when compared to microcrystalline samples, can be attributed to the phonon confinement appearing only in nanosized materials (finite size effect).[27,88]

To obtain a detailed picture of the elemental distribution throughout the bulk structure of the thin films, depth profiling by time-of-flight secondary ion mass spectrometry (ToF-SIMS) was conducted. Figure 3B presents the secondary ion (elemental) profiles of Fe^+ (red), Mg^+ (blue), Co^+ (turquoise), Ni^+ (yellow), Cu^+ (green), Si^+ (black), and C^+ (grey) as function of depth from the surface (0 nm) to the substrate interface (250 nm). The depth of the film was analyzed by profilometry after ion sputtering. The profile visualizes that copper is enriched close (first few nanometers) to the surface, while we found a slight depletion in this region for magnesium, iron, and cobalt. These enrichment and depletion effects can be explained by (classic) surface segregation effects. Furthermore, it can be stated that silicon diffuses from the (100)-oriented silicon wafer (substrate) into the bulk nanostructure. This phenomenon was already observed for other KLE-templated nanocrystalline metal oxide thin films and is explained by a diffusion-controlled migration process activated by the thermal treatment.[27,89] Quite unusual, however, is the constant Si concentration in the depth range of 20 nm to 170 nm in combination with the increase in the near surface region. This can be explained by fast diffusion on the inner pore surfaces towards the surface.

Here the diffusion is already in a steady state resulting in quite low and constant concentration within this area. The silicon, which was transported through pores (pore diffusion on inner surfaces) to the outer surface, diffuses from the surface into the bulk of the film. A comparable situation was described in literature for yttrium-stabilized zircon oxide films with columnar structure.[89] The pore diffusion in the HEF films can therefore also be considered as indirect evidence for an overall homogenous ordered through-pore structure in the whole material. The results were found to be reproducible. Most importantly, all cations were detected in almost constant concentrations between the air/HEF thin film and HEF thin film/substrate interfaces suggesting a uniform (single-phase) crystallographic structure formation and homogenous distribution of the inserted elements throughout the (bulk) thin film, which is in excellent accordance with the STEM elemental mapping and GIWAXS data (Figures 2 and 3). Only minor amounts of carbon were detected at the surface (adsorbed hydrocarbons) and within the bulk structure, which allows the conclusion that the polymeric template was almost completely combusted upon calcination at 600 °C. Since in ToF-SIMS, the chemical environment has major influence on the ionization probability (matrix effect), the slight increases of the transition metal signals at the sample/substrate interfaces can be ascribed to different local chemical environments the cations are facing in the nanoscopic vicinity of the silicon wafer rather than to an enrichment of these elements. This different chemical environment is evoked by a beam induced ion mixing effect causing a matrix, which is composed of all available interfacial components.[27]

For any catalytic processes/reactions, it is fundamental to evaluate the specific surface area of the material as it determines the number of catalytically active centers and thus the overall reactivity. Therefore, the Brunauer–Emmett–Teller (BET) surface areas were estimated by krypton physisorption measurements performed at 77 K. The underlying isotherms and corresponding BET plots show a linear correlation with the applied partial pressure (Figure S3, Supporting Information). Considering a porosity of 30%, which is a typical value reported for KLE-templated metal oxides,[18,27,74,84] and the dimensions of the thin film, the sample mass can be obtained by taking the density of ferrites into account. Based on the respective sample mass, the specific surface area of the mesoporous HEF-10 min and HEF-2 h thin films were determined to be 170 m^2 g^{-1} and 110 m^2 g^{-1}, respectively. These results are in fairly good agreement with values reported for other mesoporous metal oxides templated with KLE possessing similar mesostructures, and thus clearly indicate a porous morphology throughout the entire film.[27,74,75,90] Furthermore, the surface area of the mesostructured thin films decreased substantially during the calcination for 2 h at 600 °C, which is reasonable because of the induced crystal growth, as confirmed by TEM and GIWAXS data (Figures 2 and 3).

To elucidate the chemical composition and oxidation states of the HEF thin films, X-ray photoelectron spectroscopy (XPS) was accomplished. Figure S4A, Supporting Information displays the survey spectrum of the HEF-10 min and HEF-2 h samples revealing the photoemission signals of Fe, Co, Ni, Cu, Mg, and Zn besides the ones of carbon and oxygen. High-resolution XP spectra in **Figure** 4A exhibit the Fe 2p peaks at 710.4 eV ($2p_{3/2}$) and 724.4 eV ($2p_{1/2}$), and thus a spin-orbital splitting of 14.0 eV for both samples HEF-10 min and HEF-2 h. Satellite features were observed between 716–721 eV and 731–735 eV indicating the presence of iron in the oxidation states +2 and +3, when also taking into account the asymmetry of the photoemission peaks.[29,91] This implies that iron occupies tetrahedral and octahedral sites in the crystallographic structure. As illustrated in Figure 4B, Co 2p emission was identified to be at binding energies BE (Co $2p_{3/2}$) = 780.9 eV and BE

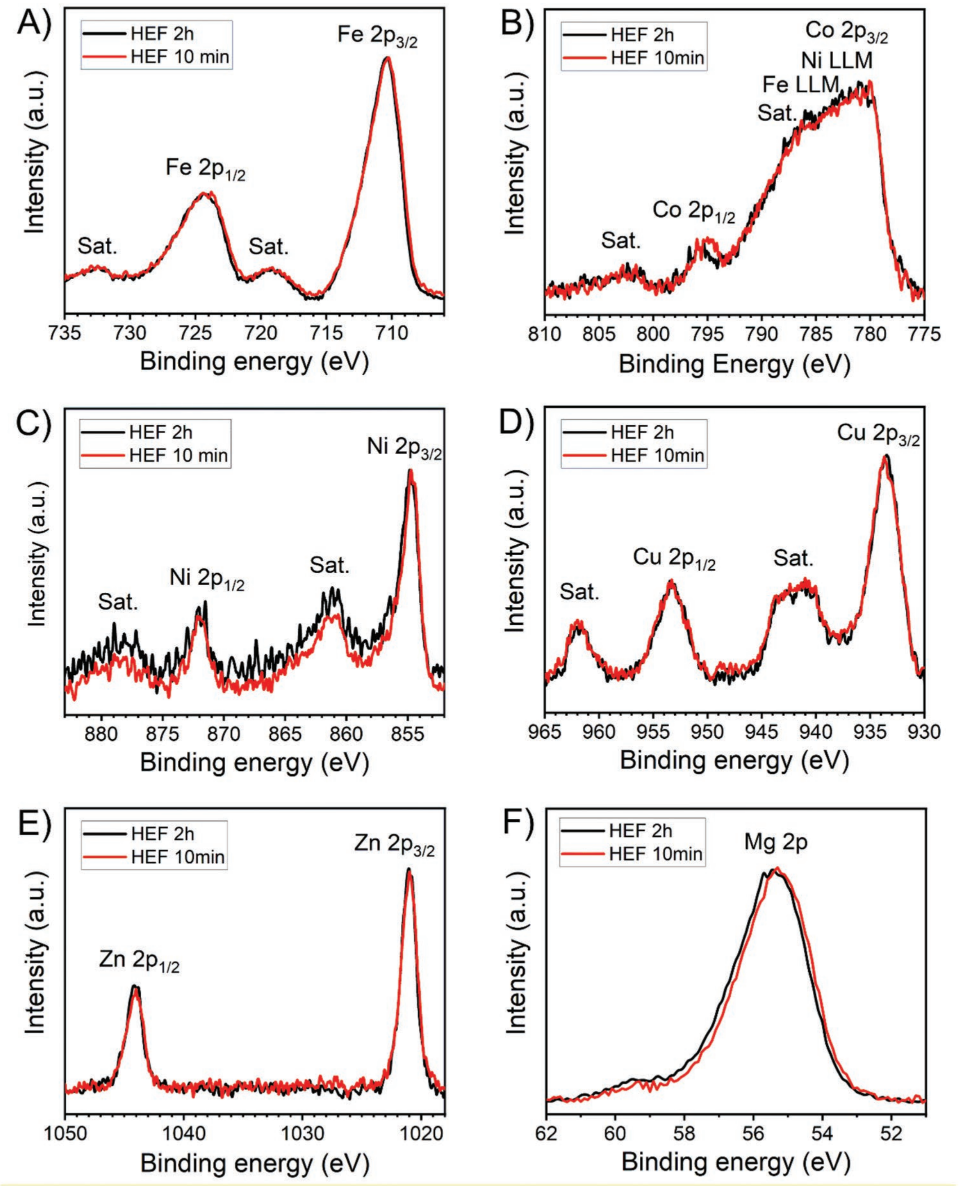

Figure 4. High-resolution XP spectra of A) Fe 2p with an overlap of Ni and Cu LMM Auger lines, B) Co 2p with a strong overlap of Ni and Fe LMM Auger lines, C) Ni 2p, D) Cu 2p, E) Zn 2p, and F) Mg 2p.

(Co $2p_{1/2}$) = 795.6 eV with satellite peak maxima at 786 eV and 803 eV both suggesting mixed valence states, which are Co^{2+} and Co^{3+}.[92] The asymmetry and too large intensity of the Co $2p_{3/2}$ peak can be predominantly attributed to overlap with the Fe and Ni LMM Auger lines, which are typically found to be at 784.0 eV and 778.0 eV, respectively, resulting in a photoemission signal, which is created by superposition of the described contributions. In the high-resolution spectra of Ni 2p (Figure 4C), two main peaks were found at 854.8 eV and 871.8 eV for the $2p_{3/2}$ and $2p_{1/2}$ orbitals (spin-orbit splitting of 17.0 eV), respectively.[93] The charge-transfer satellites between 858–862 eV and 875–885 eV observed for both samples, provide a strong hint for the presence of Ni in the oxidation states +2 and +3.[94] Additionally, the intensity ratio between the main peak and satellite is another indicator of the oxidation state. We found a ratio of area(satellite)/area(main peak) = 30% (without background subtraction). The Cu 2p region spectra are presented in Figure 4D, in which the peaks of Cu $2p_{3/2}$ are located at 933.6 eV and of Cu $2p_{1/2}$ 953.3 eV. In contrast, the emission peaks of Cu 2p do not show any asymmetry, and in combination with the satellite peaks (938–946 eV and 958–964 eV), it can be concluded that the Cu is solely incorporated as Cu^{2+} species and, therefore, can be expected to be located preferentially at tetrahedral sites in the spinel structure.[95] The two photoemission lines of Zn 2p (Figure 4E) centered at 1021 eV and 1044 eV can be attributed to Zn $2p_{3/2}$ and Zn $2p_{1/2}$, respectively, and demonstrate a spin-orbit splitting of 23.0 eV. Due to the absence of any satellite features, Zn can be expected to be exclusively in +2 state, consequently occupying tetrahedral sites in the spinel structure.[71] For the Mg 2p peak of the HEF-10 min and HEF-2 h thin films, a binding energy BE (Mg 2p) = 48.7 eV was identified (Figure 4F). The Mg $2p_{3/2}$ and Mg $2p_{1/2}$ cannot be distinguished due to a small spin-orbit splitting of 0.28 eV.[96] For both samples, the oxidation state of Mg can therefore be considered to be +2 (similar as in ZnO).[97] Interestingly, the 2p signals of all implemented metals did not show any (significant) difference in binding energies when comparing the HEF-10 min and HEF-2 h samples.

In normal spinels, the two-valent cations usually occupy 1/8 of the tetrahedral (8a) sites and the three-valent species are located at 1/2 of the octahedral (16d) interstices, whereas in inverse configurations, both sites are known to be occupied. Under consideration of the Shannon's radii[98] and the results derived from Raman spectroscopy, it can be concluded that the Mg^{2+}, Zn^{2+} and Cu^{2+} (solely present in +2 oxidation states) are located at tetrahedral and octahedral sites (partially inverse configuration). For Co, Ni, and Fe both +2 and +3 oxidation states have been found, which also suggests the occupation on tetrahedral and octahedral interstices, respectively. These findings are in good accordance with literature data.[23,28,72]

We note that the stoichiometric composition at the surface of the HEF samples was not calculated in terms of integrating the photoemission peak area and correlating the data to the elemental concentration, since we found an overlap of the Fe 2p signals with the Ni and Cu LMM Auger lines. Additionally, the Ni and Fe LMM Auger signals strongly overlap with the Co 2p spectra, wherefore we derogate from a quantitative evaluation of the surface composition. We note that in general the quantification of high entropy materials with a whole row of d-block metals of the same period is a complex task since no standardized fitting models exist, and the above-mentioned overlap of photoemission and Auger peaks do not allow for a straightforward quantification of these multi-(transition)-metallic systems by numerical integration when using a single excitation energy, such as here monochromatic Al Kα radiation (1487.6 eV). Hence, the quantification and determination of oxidation states of the inserted cations within high entropy materials (or multimetallic compounds in general) is often falsely interpreted in terms of element composition and chemical status and require in-depth synchrotron spectroscopic experiments with tunable X-ray excitation energies.

Since the C 1s signals (BE = 285.5 eV and 285.3 eV for HEF-10 min and HEF-2 h, respectively)[99] in the high-resolution spectra (Figure S4B, Supporting Information) are comparable in terms of intensity and full-width at half maximum (FWHM), the carbon emission can be ascribed to surface adsorbed hydrocarbons on the thin films rather than to be originating from residual (carbonized) KLE. Hence, the organic template can be assumed to be fully degraded after thermal treatment at 600 °C for both calcination times. This observation matches with the ToF-SIMS data showing only a slight arising of C^+ signals close to the surface (Figure 3B), whereas for KLE related carbons also C^+ signals arising from the bulk would be expected. The O 1s high-resolution spectra show a peak located at 529.7 eV (Figure S4C, Supporting Information), typically referred to bulk metal oxides.[100] The presence of a weak shoulder for binding energies in the range of 531 eV to 534 eV is indicative for low coordinated, defective oxygen species (such as oxygen vacancies, surface-adsorbed oxygen/hydroxyl groups, and surface adsorbed water).[101] Especially, the oxygen vacancies contributing to the signals of defective oxygen have been attributed to highly electro-catalytically active centers for oxygen evolution.[101,102] However, since neither a deviation with respect to the binding energy nor an asymmetry of the O 1s signal were observed, the concentration of oxygen vacancies and hydroxyl groups can be expected to be similar for the HEF-10 min and HEF-2 h mesoporous thin films. Furthermore, the detection of all initially implemented elements and the absence of any metallic impurities in the XPS spectra confirm the results obtained by the GIWAXS, TEM, EDS, and ToF-SIMS experiments.

2.2. Optical and (Photo)electrochemical Characterization

When discussing the photoelectrochemical properties of HEF, thorough investigation of the absorption characteristics is of importance as the absorption of light precedes the generation of electron-hole pairs. In essence, the absorption behavior of transition metal oxides can be explained by electronic transitions in the band structure. The actual charge transfer transitions depend on the oxidation state of the cations, d-d transition states, the nature of binding partners/atoms, the coordination geometry itself, and the heteronuclear (metal-metal) and oxygen-cation (ligand-to-metal) charge transfer transitions.[103] The band gaps of the HEF samples for direct optical transitions derived by Tauc plots were found to be at 2.3 eV and 2.7 eV for both 10 min and 2 h calcination times (**Figure 5**A). The direct (non-phonon assisted) optical transition can be ascribed to absorption of photons exciting electrons from valence band states, which are composed of overlapping oxygen 2p orbitals, and the t_{2g} levels of the 3d-states of the five distinct transition metals (assuming an octahedral coordination of M^{3+} by O^{2-} anions and resulting in an energetic splitting of the 3d configuration into low-spin (t_{2g}) and high-spin (e_g) states, which is described in detail by the ligand field theory). Both band gaps imply good absorption in the visible spectrum of light, as also visualized in the absorbance spectra (Figure S6A, Supporting Information). For an indirect (phonon-assisted) transition, band gaps of 1.0 eV, 1.4 eV, and 1.6 eV for the HEF-10 min and slightly higher values of 1.1 eV, 1.5 eV, and 1.6 eV for the HEF-2 h thin films (Figure S6B, Supporting Information), were found, also suggesting strong visible light absorption. The absorption of light in the wavelength range between 700 nm and 900 nm (Figure 5A) can be attributed to multiple low-intensity d-d transitions for the distinct transition metals (excitation of charge carriers from the t_{2g} to the corresponding e_g level).

Since the thickness of the HEF thin films is a function of the withdrawal speed of the substrate upon dip-coating, the extraction speed was doubled from 8 mm s^{-1} to 16 mm s^{-1}, which resulted in an increase of the film thickness from 190 nm to 330 nm and 230 nm to 410 nm for HEF-10 min and HEF-2 h, respectively. The increase in $(Ah\upsilon)^2$ in Figure 5A can be assigned to the stronger absorption of photons in the visible spectrum of light (1.5–3 eV) due to the increased amount of photoactive HEF.

Up to date, HEOs have rarely been characterized as photoabsorber materials for PEC water splitting. Recently, Djerdj et al. prepared rare-earth based HEOs and elucidated their

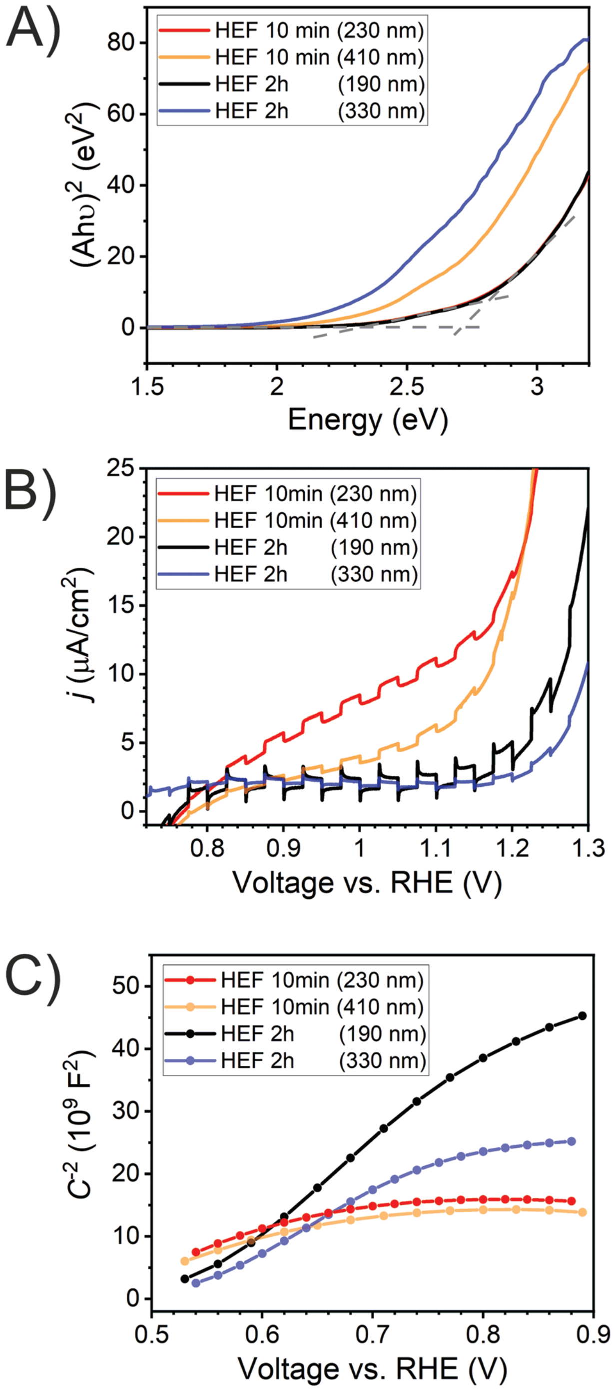

Figure 5. Optical and photoelectrochemical characterization of the mesoporous HEF-10 min and HEF-2 h thin films with distinct thicknesses: A) Tauc plots for a direct optical transition, B) chopped-light voltammetry, and C) Mott–Schottky analysis. The PEC experiments were performed in 0.1 m NaOH with a Na$_2$SO$_3$ (hole scavenger) in 3-electrode setup. Linear fitting of the MS data for estimation of the flat band potentials was conducted between 0.57–0.7 V and 0.66–0.88 V versus RHE for the HEF-10 min and HEF-2 h, respectively.

photocatalytic activity and PEC performance.[68] In their work, the best performing HEOs employed as photoanode demonstrated photocurrent densities of about 25 µA cm^{-2} at 1.23 V versus RHE (pH 13) for an optimized thickness of 3 µm. In the current study, n-type HEF thin films with thicknesses of 230 nm and 410 nm and 190 nm and 330 nm, as determined by profilometry (Figure S5, Supporting Information) for the HEF-10 min and HEF-2 h, respectively, were analyzed as photoanodes by intermittent-light voltammetry (using a white-light LED, 100 mW cm^{-2}, light/dark period 10 s) in 0.1 M NaOH with 1 M Na$_2$SO$_3$ (hole scavenger) as shown in Figure 5B. In agreement with our recent findings of PEC performance of mesoporous spinel HEOs thin film electrodes prepared with Pluronic F-127 as structure-directing agent,[23] the KLE-templated HEF samples with ordered mesopore structure also exhibited only low absolute photocurrent densities in the order of 18 µA cm^{-2} and 5 µA cm^{-2} for HEF-10 min and HEF-2 h, respectively. Interestingly, the HEF-2 h sample possesses photocurrent transients, which were absent in the HEF-10 min photoresponse. This effect can be clearly ascribed to the prolonged annealing time which results in the evolution of pronounced grain boundaries between the particles (as illustrated in Figure 2) at which recombination processes occur. The recombination of photoexcited charge carriers at these grain boundaries leads to the observed light-induced electron transport process shown in Figure 5B. Additionally, for the HEF-10 min photoanodes the dark current was found to be significantly larger than the photoconductivity, giving rise to the assumption that bulk defects dominated by transition metal d-(defect) states are involved in the electron transport. The preparation of HEF samples with increased film thickness verified these results by showing the same trend in PEC performance. Furthermore, the dark current is substantially increased for HEF-10 min compared to HEF-2 h, an effect which seems contradictive at the first glance, but can be explained by consideration of energetic splitting of the 3d states of transition metals assuming an octahedral coordination for cations in the oxidation state +3. The existence of unoccupied t$_{2g}$ levels allows the electron transport/hopping between adjacent cations. As a consequence, the electron hopping process through intrinsic defects states seems to be facilitated for the HEF-10 min related to HEF-2 h samples. This intrinsic defect based hopping mechanism also explains the near-metallic conductivity behavior. In other words, the many different d-orbital electron configurations are modified by the intrinsic property due to manifold of d-orbitals. The low PEC performance might also be affected by the increase of configurational disorder since the implementation of cations with distinct ionic radii induces stress and strain within the spinel structure. These stress and strain effects, in turn, might induce structural defects (such as point and linear defects), which impede the collection of photoexcited charge carriers owing to trapping at bulk and surface defects. During these so-called "trap-mediated" recombination processes, photogenerated electrons from the conduction band recombine with holes from the valence band states involving trap states under emission of energy.[40,104] This explanation approach also allows to describe the difference in the dark current observed for thin (230 nm and 190 nm) compared to the thicker (410 nm and 330 nm) HEF samples in Figure 5B: the increase of the film thickness results in the formation of less homogenous thin film morphologies containing more structural defects. This assumption was confirmed by intensity-modulated photocurrent spectroscopy

(IMPS), which is a powerful tool to determine charge transport dynamics by measuring the periodic photocurrent response of a photoelectrode to a small sinusoidal perturbation of the light intensity.[105] IMPS-derived Nyquist plots (Figure S8, Supporting Information) reveal a fast charge carrier transfer throughout the bulk structure with $k_{\text{trans}} = 22\ \text{s}^{-1}$, which is comparable to the charge transfer rate constants found for hematite photoanodes recorded under similar experimental conditions (pH 13 and at 1.4 V versus RHE)[106] and even exceeds the transfer rates found for $CuFe_2O_4$ photoelectrodes.[107] For the surface recombination rate constant of the underlying HEF photoanodes, a value of $k_{rec} = 17.6\ \text{s}^{-1}$ was calculated. This surface recombination rate is two to three times higher as compared to (non-porous) $CuFe_2O_4$[107] and hematite photoanodes,[106] verifying that significant surface recombination processes occur at the electrode/electrolyte interface. This observation provides the explanation—beside ultrafast bulk recombination phenomena typically occurring on the pico- and nanosecond time scale[108] and therefore not capable of being detected with this technique—for the low photocurrent density of HEF thin films. Furthermore, the photocurrent densities and IMPS data provide clear evidence that the photoresponse of thicker HEF samples does not further increase—independent of calcination time—even so the absorption of light is drastically enhanced, as was proven by UV-vis spectroscopy (Figure 5A). As consequence, the sulfite oxidation on mesoporous HEF thin films seems to be limited by the surface recombination rate, and not by the absolute amount of photogenerated charge carriers in the bulk structure. In essence, the configurational disorder induced by insertion of several cations into the spinel structure of HEF thin films, indeed results in an improved charge transfer process (see Figure 5B and 6C) based on an electron hopping mechanism via 3d states. However, this observed enhancement of the electronic conductivity for the HEF-10 min seems not to improve the PEC properties since the presence of structural defects serve—at the same time—as recombination sites for migrating (photogenerated) charge carriers. Additionally, the high degree of porosity in the HEF thin films decrease the absolute amount of photoactive mass per illuminated area, which might negatively affect the overall photoresponse, as it has also been presented for, e.g., fibrous hematite photoanodes.[88]

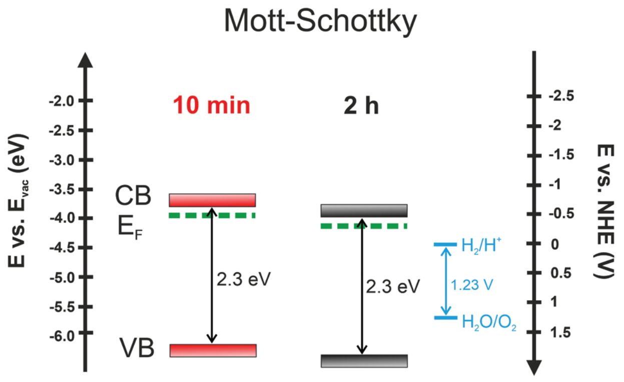

Figure 6. Energy band diagrams of the mesoporous HEF electrodes calcined at 600 °C for 10 min (red) and 2 h (black) estimated by MS analysis and under consideration of optical E_{gap} values from UV–vis spectroscopy. Energy levels are presented with respect to E_{vac} and E_{NHE}.

Conducting Mott–Schottky analysis, for an estimate of the flat band potential, φ_{FB}, positions of 0.55 V and 0.65 V versus RHE were found for the HEF-10 min and HEF-2 h electrodes, respectively (Figure 5C). It is noteworthy that onset potential (in Figure 5B) is observed to be at ca. 720 mV versus RHE, which presents a shift of 70–120 mV related to φ_{FB}. This effect is commonly observed for semiconducting photoelectrodes typically comprising a high concentration of surface defects at which charge carries accumulate (Fermi level pinning), wherefore charge carrier separation is strongly inhibited.[107,109] The flat band potentials of HEF samples are in fairly good agreement with the ones of $CuFe_2O_4$ and $ZnFe_2O_4$ which have been reported to be 0.73 eV to 0.84 eV versus RHE, respectively.[22,107] Interestingly, the HEFs have also been proven as photostable materials with a loss of relative photocurrent density of only 4.7% after repetition of 50 intermittent-light voltammetry measurements (which equals an analysis time of approximately 4 h, Figure S7, Supporting Information). In light of the fact that ferrites generally suffer from photocorrosion, and particularly $CuFe_2O_4$ is known to be photoactive for merely a few minutes under illumination due to photocorrosion,[48] it is important to highlight that high entropy materials have been currently proven to possess remarkable structural stabilities during electrochemical cyclisation. In this context, the link between configurational entropy and cycling stability of high entropy Mn-based hexacyano ferrate cathodes has been resolved.[110] The substantially improved cycling stability was attributed to the entropy-mediated suppression of phase transitions. The outcome of the (photo-) stability testing (Figure S7B, Supporting Information) in the underlying work supports the preceded findings and furthermore demonstrates that the structural stability of HEF photoelectrodes seems to be likewise improved by the high degree of compositional disorder.

A profound understanding of the energetic band alignment of semiconducting photoelectrodes is essential in order to address the question to which extent a photoabsorber is capable of driving redox reactions. In essence, the positions of the VBM, CBM, and Fermi level (E_F) under operating conditions determine the ability of a photoabsorber to reduce or oxidize water in order to produce hydrogen and oxygen, respectively. Considering the estimated flat band potentials (Figure 5C) and direct band gap energy of 2.3 eV derived from the UV-vis spectroscopy, the final energy band diagram can be drawn as shown in Figure 6. According to MS analysis, the flatband, φ_{FB}, determines the position of the Fermi level of a semiconductor (with respect to the potential of the reference electrode) in the absence of band bending and therefore reflects the thermodynamic ability of E_F to oxidize or reduce water depending of the polarity of the semiconductor.[111] Importantly, the CBM and VBM are located below the oxidation and above the reduction potentials of water, suggesting that both oxygen and hydrogen evolution can be driven theoretically by the mesoporous HEF (photo-) anodes, hence providing from a theoretical point of view suitable energy band positions for overall solar water splitting.

In order to support the experimental data and provide evidence of how the formation high entropy assisted compositions affect the electronic band structure, density functional theory (DFT) calculations were conducted on HEF and MEF. The valence and conduction band edge levels versus the vacuum

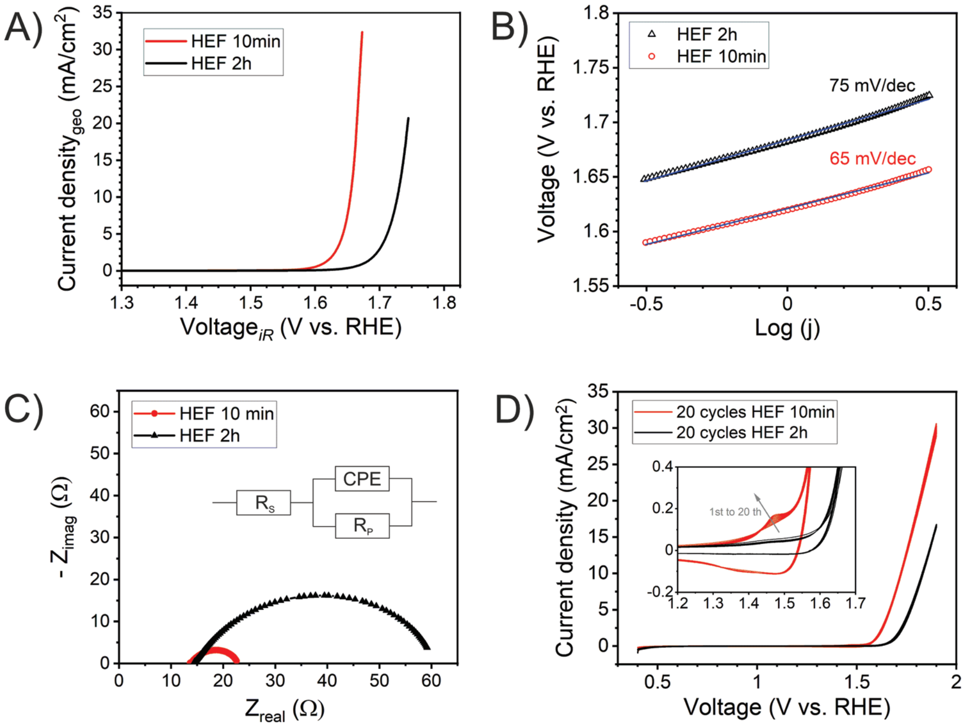

Figure 7. Electrochemical characterization of mesoporous HEF thin films calcined at 600 °C for 10 min (red) and 2 h (black): A) LSV curves (scan rate 10 mV s^{-1}) plotted against the *iR*-corrected voltage, B) Tafel plots with the corresponding linear fitting, C) Nyquist plots measured at 1.7 V, and D) 20 consecutive CV curves recorded with 50 mV s^{-1} and an inlet showing a magnification of the potential window between 1.2 V and 1.7 V. All experiments were accomplished in 1 м KOH and a 3-electrode-setup with the voltage plotted against RHE.

level were computed for the cubic spinel ferrite compositions $Co_4Ni_4Cu_5Zn_5Fe_{36}O_{72}$ (MEF) and $Mg_4Co_3Ni_3Cu_4Zn_4Fe_{36}O_{72}$ (HEF) in their ferromagnetic states, in which all Fe cations occupy the octahedral site and other cations occupy the tetrahedral site (cf. Figure S9, Supporting Information).[112–114] For the HEF and MEF, valence band maxima of -6.35 eV and -4.51 eV were obtained, respectively. The DFT derived VBM agree with the Mott–Schottky data and confirm that the HEFs are in principle capable of performing unassisted water oxidation, while the MEF are not, due to positioning of the VBM above the oxidation potential of water (see Figure 6 and Figure S9, Supporting Information). In consequence, the incorporation of Mg into the spinel structures shifts the VBM upward in energy. Because DFT calculations based on the generalized gradient approximation (GGA) level generally underestimate the band gap energy, the position of the CBM has limited meaning. For the HEF and MEF, we obtain band gaps of 0.48 eV and 0.39 eV, respectively, which are in good accordance to theoretical calculations on $NiFe_2O_4$ showing an indirect band gap energy of ≈ 0.5 eV.[112]

2.3. Oxygen Evolution Reaction Activity

In order to elucidate the influence of calcination time on the electrocatalytic water oxidation activity, the mesoporous HEF-10 min and HEF-2 h thin films were electrochemically characterized. Linear sweep voltammetry curves of the calcined HEF thin films (measured in 1 м KOH) are depicted in **Figure 7**A. The shorter calcined (10 min) sample showed a significantly lower overpotential of 420 mV at 10 mA cm^{-2} as compared to the 500 mV at 10 mA cm^{-2} for HEF-2 h. For comparison, the HEF-10 min sample possesses superior performance over the structurally related mesoporous $NiFe_2O_4$ (calcined at 550 °C, $\eta > 570$ mV at 10 mA cm^{-2})[57] and Ni foil investigated under identical conditions (Figure S10A, Supporting Information). These potentials (versus RHE) were *iR*-corrected through identifying the electrolyte resistance R_S from the Nyquist plots, which were evaluated to be 13.7 Ω and 14.5 Ω for the HEF-10 min and HEF-2 h thin films, respectively. The observed overpotentials are in a typical range also found for other spinel-type OER catalysts.[53] Comparing the Tafel plots (Figure 7B), the slopes for the HEF-10 min and HEF-2 h samples were found to be 65 mV dec^{-1} and 75 mV dec^{-1}, respectively, indicating enhanced reaction kinetics at the electrode/electrolyte interface for the shorter calcined material. These results are supported by electrochemical impedance spectroscopy (EIS) analysis. The Nyquist plots exhibited in Figure 7C show a lower charge transfer resistance of only 23 Ω for the HEF-10 min as compared to 60 Ω for HEF-2 h. This result is surprising at a first glance, since the latter sample has been shown to be more crystalline (by HR-TEM and GIWAXS), therefor one would expect an increased conductivity. For the explanation two reason can be found: firstly, the preservation of a well-defined (three-dimensional) mesopore network, in which the connectivity of nanograins and with that the connection of electronic conduction paths is retained for HEF-10 min (see Figure 2). This assumption is in good agreement with the finding of Hartmann et al. proving that an ordered mesoporous network composed of sol-gel derived TiO_2 is the origin for enhanced electronic conductivity and low charge carrier recombination.[77] Secondly (and corroboratively), the improved OER performance can be related to the higher electric conductivity, which, in turn, is the consequence of a higher number of d-electron states in the material allowing electron hopping processes between the iso-energetic states.

The retention of the mesopore architecture after annealing at 600 °C for only 10 min can also be considered as an explanation for the greatly increased double-layer capacitance, C_{DL}, which was found to be more than 4 times larger (4.3 mF cm^{-2}) as compared to the longer calcined samples (1 mF cm^{-2}). This is in accordance with the BET surface areas, which was highest for the HEF-10 min thin film. The cyclic voltammetry (CV) plots for both samples recorded at distinct scan rates and the corresponding linear regression (fitting) for determination of the C_{DL}[115] can be found in the Supporting Information in Figure S10B–D, Supporting Information. The capability of completely infiltrating an ordered mesoporous metal oxide network by a cobalt nitrate solution was shown for TiO_2 thin films and proven by ToF-SIMS analysis.[77] It can be expected that the same physical process is valid for the mesoporous HEF thin films when coming in contact with the aqueous electrolyte. Additionally the presence of mesopores is expected to promote the escape of evolved oxygen bubbles and facilitate the diffusion and transport of reactive species (such as hydroxides).[77,115] Conclusively, the aqueous electrolyte in the underlying work is very likely to be penetrated throughout the HEF mesopore framework and thus contributing to a high double-layer capacitance, which in turn is known to directly correlate with the electrochemical active surface area.[116]

The CV curves in Figure 7D not only demonstrate a difference in the absolute current density between HEF-10 min and HEF-2 h, they also show the appearance of an oxidation peak around 1.45 V and reductive deflection of the curve between 1.55 to 1.2 V versus RHE for the HEF-10 min thin film. The oxidation peak increases in intensity upon cyclisation from the 1st to the 20th cycle. This trend can be interpreted as an oxidation process which occurs at the surface of the electrocatalyst under prolonged operation, most likely attributable to the oxidation of cations with the oxidation state +2 being oxidized to +3. Furthermore, the rise of the oxidation peak implies a more redox reactive surface and thus a less stable structure—which is plausible since the HEF-10 min thin film possesses a higher surface area and lower crystallinity. When analyzing both HEF materials at a constant current density of 10 mA cm^{-2} for 1 h (chronopotentiometry, Figure S10E, Supporting Information), the HEF-10 min and HEF-2 h materials showed a decrease of the overpotentials by 10 mV and 15 mV over operation time, respectively. In essence, the materials can be considered as stable electrocatalysts for at least 1 h in fact showing an improvement of OER activity over time.

Since the precise evaluation of the electronic structure of transition metal oxides is an intricate interplay between the adsorption energy of the adsorbate (e_g occupancy), the covalency (O 2p energy levels), and the interface energetics, requiring usually synchrotron-based spectroscopic tools for detailed evaluation, we chose the degree of crystallinity and surface area as the two main control parameters to discuss the differences in OER activity. The most reactive species in spinels can be considered 3+ cations typically occupying octahedral sites (in a regular spinel configuration). The improved electrocatalytic activity of octahedrally as compared to tetrahedrally coordinated cations have recently been summarized in a review article.[54] Octahedrally coordinated metals are the redox-active centers in spinels for three reasons: 1) an effective interaction of the cations with the oxygen atoms (TMO_6 octahedron) is ensured, 2) adjacent octahedral sites interact cooperatively in promoting the OER kinetics, and 3) a preferential exposure of octahedral cations on the surface is given.[54] Additionally, the degree of crystallinity correlates with OER activity since amorphous structures typically possess more structural defects, which are known for effecting the electronic band structure and surface energetics, and in turn determine the adsorption energy of reaction intermediates.[117] In this context, in TM oxides the formation of oxygen vacancies becomes dominant in determining the OER steps described by the LOM mechanism.[65] In recent studies, oxygen vacancies have been found as main impact factor for the OER performance of mesoporous (sol-gel-derived) HEO thin films, which was correlated with the increase in surface area.[23] In the underlying work, the shoulder in the O 1s signal (Figure S4C, Supporting Information) was determined to be—independent of the surface area—the same in binding energy and shape indicative for a comparable concentration of defective oxygen and/or hydroxy groups. In conclusion, the enhanced OER activity of the HEF-10 min sample over HEF-2 h can be assigned to both a higher electric conductivity and a higher specific surface area (BET surface area: 170 m^2 g^{-1} versus 110 m^2 g^{-1}). Kr physisorption experiments and the difference in double-layer capacitance indicate a largely increased surface area of the HEF-10 min mesoporous thin films, therefore offering significantly more catalytically reactive centers in the form of octahedrally coordinated Co^{3+} and Ni^{3+}. The presence of the highly catalytically active species were confirmed by XPS (Figure 4) and can be expected to be located at octahedral sites, which were described to be exposed preferentially at the surface.[54]

3. Conclusion

In this work, nanocrystalline and ordered mesoporous high entropy ferrite (HEF) thin films have been synthesized by a sol-gel based dip-coating approach and subsequent calcination at 600 °C for either 10 min or 2 h. KLE as a porogen promotes the formation of uniform and homogenous (crack-free) thin films hosting periodically ordered mesopores forming a nanoarchitecture with high surface areas, up to 170 m^2 g^{-1} (by Kr-physisorption). The implementation of six distinct transition metal precursors during the soft-templating process yielded a novel nanostructured $CoNiCuZnMgFe_2O_4$ compound crystallizing in the spinel structure (evaluated by TEM and GIWAXS). The cations were shown to be homogenously distributed within the HEF thin films even on the nanoscale, results which were supported by TEM based EDS and ToF-SIMS investigations. Both methods proved the uniform distribution of inserted elements throughout the bulk structure. XPS data demonstrated the presence of Mg, Zn, Cu in 2+ states and Fe, Ni, Co being in 2+/3+ mixed valence states. The HEF electrodes have been shown to efficiently absorb light in the visible spectrum (UV-vis spectroscopy). The upward shift of the VBM due to substitution by Mg on the A-cation site was confirmed by DFT calculations. When characterized as photoanode, only low photocurrent densities (1–2 μA cm^{-2}) were found due to incorporation of structurally-related recombination sites. Investigation of the electrocatalytic activity in alkaline solution revealed promising overpotentials of 420 mV and 500 mV at 10 mA cm^{-2} for samples which were calcined for 10 min and 2 h, respectively. The improved electrocatalytic activity of shorter calcined (10 min) samples as compared to longer calcined (2 h) samples is ascribed to higher specific surface areas and higher electronic conductivities rather than to the chemical environment on the surface. The OER activity can be generally assigned to octahedrally coordinated Ni^{3+} and Co^{3+}. In essence, it can be concluded that the calcination time affects both the PEC and the OER performance of the mesoporous HEF thin films. A lower calcination time is beneficial for the development of a less defined electronic structure of the mesoporous HEF thin films, which leads to improved charge carrier transport properties (electron hopping through d-d states) as confirmed by EIS. The underlying work presented a general synthetic concept for the controlled and reproducible preparation of ordered mesoporous high entropy ferrite thin films readily available on conductive substrates and further addressed the fundamental impact of a nanoscale framework on these relevant properties. Further optimization of the mesoporous HEF thin films might be achieved by modification of the elemental composition and tailoring the pore and nanocrystal size of the material—both (synthetic) attempts known to have impact on the charge carrier transport and electronic structure. The formation of mesoporous HEF thin films with less grain boundaries might also be an important structural feature which has to be considered in order to enhance the PEC performance of mesostructured materials. Conclusively, this novel high entropy oxide class can be considered as interesting candidate and nanostructure for energy applications where high surface-areas offering a large number of (catalytically) active reaction sites are advantageous.

4. Experimental Section

Materials: All chemicals were of analytical grade and used as received: magnesium (II) nitrate anhydrous (99.999%, Sigma Aldrich), zinc (II) nitrate hexahydrate (≥99.0%, Sigma Aldrich), iron (II) nitrate nonahydrate (≥99.95%, Sigma Aldrich), cobalt (II) nitrate hexahydrate (99.999%, Sigma Aldrich), nickel (II) nitrate hexahydrate (99.999%, Sigma Aldrich), copper nitrate hemi(pentahydrate) (≥99.99%, Sigma Aldrich), sodium sulfite (≥98.0%, anhydrous, Carl Roth), 1 м KOH (Carl Roth), ethanol (EtOH, ≥99.8%, Carl Roth), and 2-methoxyethanol (2-ME, ≥99.5%, Sigma Aldrich). Poly(ethylene-*co*-butylene)-*block*-poly(ethylene oxide) (KLE) was synthesized as reported in literature[25]; molar mass 7.8 kg mol^{-1}, 42 wt% ethylene oxide, dispersity 1.04 (by ^{1}H NMR spectroscopy and size exclusion chromatography).

Mesoporous HEF Thin Film Preparation: The preparation of the dip-coating solution was inspired by Brezesinski et al.[29] The modified synthesis was optimized as follows: 22 mg $Mg(NO_3)_2 \times H_2O$, 26 mg $Zn(NO_3)_2$ 6 H_2O, 350 mg $Fe(NO_3)_3$ 9 H_2O, 25 mg $Co(NO_3)_2$ 6 H_2O, and 25 mg $Ni(NO_3)_2$ 6 H_2O, and 20 mg $Cu(NO_3)_2 \cdot 2.5\ H_2O$ were dissolved in 1 mL EtOH and 45 mg of KLE was dissolved in a mixture of 0.7 mL of 2-ME and 0.6 mL EtOH. Both solutions were vigorously stirred over 30 min (until homogenous solution was obtained) and were subsequently mixed dropwise and stirred for another hour. After stirring, the solution was treated in an ultrasonication bath for 5 min. Prior dip-coating, all substrates were cleaned for 15 min with ethanol and acetone assisted by ultrasonication. Dip-coating was conducted with a dip-coater from Ossila. In a water-free container, fluorine-doped SnO_2 (FTO, *XOP glass*) and silicon (100) wafers (Siltronic) were used as substrates, which were withdrawn with a constant speed of 4–8 mm s^{-1}. Optimum conditions in terms of formation of a well-developed mesoporous network were found for a relative humidity between 10 and 18%. After dip-coating, the samples were transferred into a pre-heated muffle furnace (Nabertherm LT3/11) and heated to 260 °C (heat rate of 1 °C min^{-1}) and hold at this temperature for 15 h. This stabilization step was followed by rapid heating to 600 °C (with a heating ramp of 10 °C min^{-1}) and kept at this temperature for 10 min and 2 h, respectively.

Structural Characterization: SEM investigations were carried out on a Philips XL30 FEG at acceleration voltages of 30 keV and working distances between 5 and 10 cm. EDS based elemental analysis was accomplished with a SEM instrument from JEOL (JSM 7600F) equipped with an EDS detector from Oxford Instruments (X-Max 80). Using a razor blade, flakes of the thin film were scraped off the silicon substrate and collected in a small sample glass. After adding two ml of ethanol, they were dispersed with the help of an ultrasonic bath. The dispersion is allowed to settle for 20 s to separate large particles. Two to three droplets of the upper part of the dispersion were applied on a carbon coated copper grid (holey type, Plano GmbH, Wetzlar). After evaporation of the ethanol, the samples were coated with a thin carbon film (carbon coater MED 010, Bal-Tec AG, Balzers, Liechtenstein) to eliminate charging from the incident electron beam in the TEM. Examination of the samples were performed using the TEM and STEM mode in a FEG TEM (JEM2100F, JEOL Ltd., Tokyo, Japan). For recording EDS maps, an Oxford X-Max 80 EDS detector (Oxford Instruments NanoAnalysis & Asylum Research, High Wycombe, United Kingdom) was used. Krypton physisorption measurements (on FTO deposited HEF thin films) were accomplished at 77.35 K using an *Autosorb iQ* by *Quantachrome Instruments*. The thin films were annealed at 200 °C for 6 h before, in order to desorb attached water. The obtained data were analyzed with the *ASiQwin* Software based on the BET model and a multi-point evaluation procedure. Values for the specific surface area were finally received by determination of the sample's mass with the aid of the calculated thin film area, thickness (determined by profilometry), and knowing the density of ferrites including an assumed porosity of 30% (consistently reported for KLE-based metal oxides in literature).[17,27,74,84] GIWAXS was conducted on a Rigaku Smartlab (Cu Kα radiation) diffractometer in a grazing incidence setup with $\theta_{\text{source}} = 5°$. Data were recorded between 10° and 60° (in units of 2θ) using a step size of 0.01°. The film thicknesses were determined with a Bruker profilometer (Dektak XT) using a scan rate of 10 μm s^{-1} and a stylus force of 5 mg.

Spectroscopic Characterization: X-Ray photoelectron spectroscopy experiments were accomplished in a vacuum-cluster tool on a ULVAC-PHI VersaProbe II instrument with a base pressure in the analysis chamber below $5 \cdot 10^{-9}$ mbar. Monochromatized Al K_α radiation (1486.6 eV) was utilized as excitation source. Detail spectra were measured applying a pass energy of 23.5 eV and a step size of 0.1 eV per step. The sp^3 component in the C 1s spectrum was set to 285.0 eV and all other binding energies were calibrated accordingly. Backgrounds of the acquired spectra were subtracted by using the Shirley method in CasaXPS,[118] version 2.3.25. TOF-SIMS depth profiling was performed using an M6 Hybrid SIMS (IONTOF Company, Münster, Germany). The machine was operated in dual beam mode. For analysis scans 30 keV Bi^+ ions were used and for sputtering 1 keV O_2^+ ions. With the sputter beam (I = 232.6 nA) a 300 × 300 μm^2 crater was produced. Analysis scans were done in positive polarity on an area of 150 × 150 μm^2 centered to the sputter crater. The primary ion current was I = 1.281 pA at a cycle time of 100 µs. By using the spectrometry mode for the Bi gun, a mass resolution $m/\Delta m > 9500$ (FWHM) was achieved for Ni as well as Co.

An electron flood gun produced low energetic electrons for charge compensation. The measurement was stopped at the film-substrate interface and the crater depth was measured with a stylus profiler Alpha-Step D-600 (KLA Tencor) and used for depth calibration. The repetition of the measurement showed the same homogeneous film composition. Raman spectra were acquired with a LabRAM Horiba HR-800 Raman microscope with a 514 nm laser. Using a neutral density filter the power density was 25 mW at a spot size of ≈1.5 µm for a 50x LWD objective. As a 600 gr mm^{-1} grating was chosen, the diameter of the pinhole was set to 200 µm and the entrance slit size to 100 µm. Spectra were accumulated 15 times for 10 s acquisition time per scan. For each sample equivalent spectra were collected on two different positions.

Optical Characterization: UV-visible light spectroscopy was accomplished by a UV/Vis/NIR spectrometer from PerkinElmer (Lambda 950). The absorption spectra were determined by measuring the transmittance between 320 nm and 1200 nm using a scan speed of 500 nm min^{-1} and a data interval of 2 nm. By conversion of the corresponding absorbance spectra into the Tauc plots, the direct and indirect optical band gaps were derived by extrapolation of the slope with the intercept of the x-axis and the baseline of the plot, respectively.

DFT Calculations: Band structure calculations were performed employing the Vienna ab initio Simulation Package (VASP),[119,120] using a cutoff energy of 400 eV. To simulate the quasirandom cation distribution in the high-entropy spinel ferrites, we employed $(\sqrt{3/2}\times\sqrt{3/2}\times\sqrt{3})R100.5^\circ$ super cells of the cubic spinel structure with 126 atoms in total. Quasirandom distributions of 4 Co, 4 Ni, 5 Cu, 5 Zn atoms for the medium-entropy composition and 4 Mg, 3 Co, 3 Ni, 4 Cu, and 4 Zn atoms for the high entropy composition were generated using the special quasirandom structures (SQS) method as implemented in sqsgen,[121] where Fe occupies the octahedral sites, and the other cations are distributed quasirandomly over the tetrahedral sites. Gamma-point-centered (5 × 5 × 3) k-meshes were used for the super cell calculations. To account for the local electron correlation at the transition metal cation sites, a Hubbard-correction of 4.5 eV,[112] 4 eV,[112] and 5 eV,[113,114] was applied to Fe, Co, Ni, and Cu, respectively. The DOS and absolute band alignment of unrelaxed cells in ferromagnetic state were computed by correcting the band energies by the averaged bulk potential versus the vacuum potential.

Electrochemistry: All electrochemical experiments were conducted in a three-electrode setup (Zahner cell PECC-2) utilizing a Hg/HgO reference electrode and a platinum wire ring as counter electrode. The electrolyte was chosen to be 1 m KOH (pH ≈ 13.6) including 1 m Na_2SO_3. The potential was controlled by a GAMRY Interface 1000E potentiostat. Linear sweep voltammetry (LSV) was acquired between 0.9 V and 1.9 V versus RHE using a step size of 1 mV and a scan rate of 10 mV s^{-1}. Cyclic voltammetry (CV) was conducted between 0.4 V and 1.8 V versus RHE with a scan rate of 50 mV s^{-1} and a step size of 1 mV. The potentials in the LSV curves were corrected by *iR*-drop through evaluation of the electrolyte resistance derived from electrochemical impedance spectroscopy (EIS) data. The double-layer capacitance was derived after the method of McCrory[122] by analyzing the differential current densities for distinct scan rates of 10–50 mV s^{-1} in a non-faradaic potential range (between 1.2 V and 1.4 V versus RHE). EIS was measured at 1.7 eV versus RHE for applied frequencies between 100 kHz and 1 Hz and by using an AC modulation of 10 mV. Chronopotentiometry was carried out at constant current density of 10 mA cm^{-2} for 3600 s. The reference potential of the Hg/HgO electrode was measured against a reversible hydrogen electrode (RHE, HydroFlex, Gaskatel) in the above-mentioned electrolyte before the experiments and used as conversion value taken the Nernst-equation into account.

Photoelectrochemical characterization was performed in a three-electrode setup (PECC-2 cell from Zahner Elektrik GmbH) in 0.1 M NaOH with 1 M Na_2SO_3 (hole scavenger, pH of electrolyte ≈ 12.9) employing the mesoporous HEF films on FTO as working electrode, a platinum wire as counter electrode, and Hg/HgO (stored in 1 M NaOH) as reference electrode. The applied potentials for all methods were controlled by a Zahner Zennium potentiostat (P211). As light source a white light LED was utilized (λ_{max} = 536 nm, P = 100 mW cm^{-2}) illuminating the PEC cell from a distance of 10 cm. For IMPS experiments, the same white-light LED was used operating at an average intensity of 800 mW cm^{-2} and applying a peak amplitude of 200 mV in a modulation frequency range between 10 kHz to 200 mHz. The Nyquist plot under sinusoidally perturbated illumination was recorded at 1.4 V versus RHE in 0.1 m NaOH and in the same setup configuration as described in the previous section.

Statistical Analysis: For statistical evaluation of the EDS data, 17 distinct spots on the mesoporous HEF thin films (deposited on FTO) were analyzed and averaged. According to the averaged value, the standard deviation (SD) was calculated as shown in Table S1, Supporting Information. For the DFT calculations a quasirandom cation distribution in the high-entropy spinel ferrites was employed using $\left(\sqrt{3/2}\times\sqrt{3/2}\times\sqrt{3}\right)R100.5^\circ$ super cells of the cubic spiel structure with 126 atoms in total. Quasirandom distributions of 4 Co, 4 Ni, 5 Cu, 5 Zn atoms for the medium-entropy composition and 4 Mg, 3 Co, 3 Ni, 4 Cu, and 4 Zn atoms for the high entropy composition were generated using the special quasirandom structures (SQS) method, where Fe occupies the octahedral sites, and the other cations are distributed over the tetrahedral sites. Gamma-point-centered (5 × 5 × 3) k-meshes were used for the super cell calculations. The DOS and absolute band alignment of unrelaxed cells in ferromagnetic state were computed by correcting the band energies by the averaged bulk potential versus the vacuum potential.

Supporting Information

Supporting Information is available from the Wiley Online Library or from the author.

Acknowledgements

The authors acknowledge Ulrike Kunz, Christian Dietz, and Nils Schäfer, all members of TU Darmstadt, for measuring EDS, assisting in AFM analysis, and support with GIWAXS characterization, respectively. The authors thank Alexander Kafka for help with DFT calculations. This work was funded by the Deutsche Forschungsgemeinschaft (DFG, German Research Foundation, Walter Benjamin Programm to M. Einert) under project no. 469377211. Julia Gallenberger and Jan Philipp Hofmann acknowledge financial support from BMBF, the German Ministry for Science and Education, under project no. 03HY105H. Chuanmu Tian acknowledges financial support from China Scholarship Council (no. 202008420222).

Open access funding enabled and organized by Projekt DEAL.

Conflict of Interest

The authors declare no conflict of interest.

Data Availability Statement

The data that support the findings of this study are available from the corresponding author upon reasonable request.

Keywords

high entropy oxides, mesoporous, oxygen evolution reaction (OER), photoelectrochemical, water splitting

Received: September 1, 2022
Revised: December 19, 2022

[1] Y. Ma, Y. Ma, Q. Wang, S. Schweidler, M. Botros, T. Fu, H. Hahn, T. Brezesinski, B. Breitung, *Energy Environ. Sci.* **2021**, *14*, 2883.
[2] A. Sarkar, Q. Wang, A. Schiele, M. R. Chellali, S. S. Bhattacharya, D. Wang, T. Brezesinski, H. Hahn, L. Velasco, B. Breitung, *Adv. Mater.* **2019**, *31*, 1806236.
[3] C. M. Rost, E. Sachet, T. Borman, A. Moballegh, E. C. Dickey, D. Hou, J. L. Jones, S. Curtarolo, J.-P. Maria, *Nat. Commun.* **2015**, *6*, 8485.
[4] L. Lin, K. Wang, A. Sarkar, C. Njel, G. Karkera, Q. Wang, R. Azmi, M. Fichtner, H. Hahn, S. Schweidler, *Adv. Energy Mater.* **2022**, *12*, 2103090.
[5] J. Gild, M. Samiee, J. L. Braun, T. Harrington, H. Vega, P. E. Hopkins, K. Vecchio, J. Luo, *J. Eur. Ceram. Soc.* **2018**, *38*, 3578.
[6] P. Sarker, T. Harrington, C. Toher, C. Oses, M. Samiee, J.-P. Maria, D. W. Brenner, K. S. Vecchio, S. Curtarolo, *Nat. Commun.* **2018**, *9*, 4980.
[7] L. Wu, J. P. Hofmann, *Curr. Opin. Electrochem.* **2022**, *34*, 101010.
[8] D. Berardan, A. K. Meena, S. Franger, C. Herrero, N. Dragoe, *J. Alloys Compd.* **2017**, *704*, 693.
[9] A. Sarkar, L. Velasco, D. Wang, Q. Wang, G. Talasila, L. de Biasi, C. Kübel, T. Brezesinski, S. S. Bhattacharya, H. Hahn, *Nat. Commun.* **2018**, *9*, 1.
[10] T. X. Nguyen, Y.-H. Su, C.-C. Lin, J. Ruan, J.-M. Ting, *Adv. Sci.* **2021**, *8*, 2002446.
[11] X. Xu, Z. Shao, S. P. Jiang, *Energy Technol.* **2022**, *10*, 2200573.
[12] J. S. Kim, B. Kim, H. Kim, K. Kang, *Adv. Energy Mater.* **2018**, *8*, 1702774.
[13] Y. Sun, S. Dai, *Sci. Adv.* **2021**, *7*, eabg1600.
[14] J. Dąbrowa, M. Stygar, A. Mikuła, A. Knapik, K. Mroczka, W. Tejchman, M. Danielewski, M. Martin, *Mater. Lett.* **2018**, *216*, 32.
[15] S. H. Albedwawi, A. AlJaberi, G. N. Haidemenopoulos, K. Polychronopoulou, *Mater. Des.* **2021**, *202*, 109534.
[16] C. J. Brinker, Y. Lu, A. Sellinger, H. Fan, *Adv. Mater.* **1999**, *11*, 579.
[17] E. Celik, Y. Ma, T. Brezesinski, M. T. Elm, *Phys. Chem. Chem. Phys.* **2021**, *23*, 10706.
[18] T. Brezesinski, D. Fattakhova Rohlfing, S. Sallard, M. Antonietti, B. M. Smarsly, *Small* **2006**, *2*, 1203.
[19] T. Brezesinski, J. Wang, J. Polleux, B. Dunn, S. H. Tolbert, *J. Am. Chem. Soc.* **2009**, *131*, 1802.
[20] T. E. Quickel, H. van Le, T. Brezesinski, S. H. Tolbert, *Nano Lett.* **2010**, *10*, 2982.
[21] Y. Wang, T. Brezesinski, M. Antonietti, B. Smarsly, *ACS Nano* **2009**, *3*, 1373.
[22] K. Kirchberg, S. Wang, L. Wang, R. Marschall, *ChemPhysChem* **2018**, *19*, 2313.
[23] M. Einert, M. Mellin, N. Bahadorani, C. Dietz, S. Lauterbach, J. P. Hofmann, *ACS Appl. Energy Mater.* **2022**, *5*, 717.
[24] B. Smarsly, M. Antonietti, *Eur. J. Inorg. Chem.* **2006**, *2006*, 1111.
[25] A. Thomas, H. Schlaad, B. Smarsly, M. Antonietti, *Langmuir* **2003**, *19*, 4455.
[26] J.-M. Wu, I. Djerdj, T. von Graberg, B. M. Smarsly, *Beilstein J. Nanotechnol.* **2012**, *3*, 123.
[27] K. Brezesinski, J. Haetge, J. Wang, S. Mascotto, C. Reitz, A. Rein, S. H. Tolbert, J. Perlich, B. Dunn, T. Brezesinski, *Small* **2011**, *7*, 407.
[28] J. Haetge, C. Suchomski, T. Brezesinski, *Inorg. Chem.* **2010**, *49*, 11619.
[29] C. Reitz, C. Suchomski, J. Haetge, T. Leichtweiss, Z. Jagličić, I. Djerdj, T. Brezesinski, *Chem. Commun.* **2012**, *48*, 4471.
[30] C. Reitz, C. Suchomski, V. S. K. Chakravadhanula, I. Djerdj, Z. Jagličić, T. Brezesinski, *Inorg. Chem.* **2013**, *52*, 3744.
[31] Y. Yang, S. Niu, D. Han, T. Liu, G. Wang, Y. Li, *Adv. Energy Mater.* **2017**, *7*, 1700555.
[32] J.-W. Jang, D. Friedrich, S. Müller, M. Lamers, H. Hempel, S. Lardhi, Z. Cao, M. Harb, L. Cavallo, R. Heller, *Adv. Energy Mater.* **2017**, *7*, 1701536.
[33] X. Zhou, H. Dong, *ChemCatChem* **2019**, *11*, 3688.
[34] F. F. Abdi, T. J. Savenije, M. M. May, B. Dam, R. van de Krol, *J. Phys. Chem. Lett.* **2013**, *4*, 2752.
[35] A. Fujishima, K. Honda, *Nature* **1972**, *238*, 37.
[36] M. Einert, P. Hartmann, B. Smarsly, T. Brezesinski, *Sci. Rep.* **2021**, *11*, 17687.
[37] I. Cesar, K. Sivula, A. Kay, R. Zboril, M. Grätzel, *J. Phys. Chem. C* **2009**, *113*, 772.
[38] A. Tacca, L. Meda, G. Marra, A. Savoini, S. Caramori, V. Cristino, C. A. Bignozzi, V. G. Pedro, P. P. Boix, S. Gimenez, *ChemPhysChem* **2012**, *13*, 3025.
[39] S. P. Berglund, D. W. Flaherty, N. T. Hahn, A. J. Bard, C. B. Mullins, *J. Phys. Chem. C* **2011**, *115*, 3794.
[40] M. Einert, T. Weller, T. Leichtweiß, B. M. Smarsly, R. Marschall, *ChemPhotoChem* **2017**, *1*, 326.
[41] A. Wolcott, W. A. Smith, T. R. Kuykendall, Y. Zhao, J. Z. Zhang, *Adv. Funct. Mater.* **2009**, *19*, 1849.
[42] J. H. Kim, H. E. Kim, J. H. Kim, J. S. Lee, *J. Mater. Chem. A* **2020**, *8*, 9447.
[43] K. Sivula, F. L. Formal, M. Grätzel, *ChemSusChem* **2011**, *4*, 432.
[44] A. G. Tamirat, J. Rick, A. A. Dubale, W.-N. Su, B.-J. Hwang, *Nanoscale Horiz.* **2016**, *1*, 243.
[45] Y. Lin, G. Yuan, S. Sheehan, S. Zhou, D. Wang, *Energy Environ. Sci.* **2011**, *4*, 4862.
[46] F. E. Osterloh, *Chem. Soc. Rev.* **2013**, *42*, 2294.
[47] I. Roger, M. A. Shipman, M. D. Symes, *Nat. Rev. Chem.* **2017**, *1*, 0003.
[48] S. Park, J. H. Baek, L. Zhang, J. M. Lee, K. H. Stone, I. S. Cho, J. Guo, H. S. Jung, X. Zheng, *ACS Sustainable Chem. Eng.* **2019**, *7*, 5867.
[49] R. A. Henning, P. Uredat, C. Simon, A. Bloesser, P. Cop, M. T. Elm, R. Marschall, *J. Phys. Chem. C* **2019**, *123*, 18240.
[50] A. Bloesser, J. Timm, H. Kurz, W. Milius, S. Hayama, J. Breu, B. Weber, R. Marschall, *Sol. RRL* **2020**, *4*, 1900570.
[51] S. Chen, D. Huang, P. Xu, W. Xue, L. Lei, M. Cheng, R. Wang, X. Liu, R. Deng, *J. Mater. Chem. A* **2020**, *8*, 2286.
[52] M. H. Mendonça, M. I. Godinho, M. A. Catarino, M. I. Da Silva Pereira, F. M. Costa, *Solid State Sci.* **2002**, *4*, 175.
[53] H. Wang, K. H. L. Zhang, J. P. Hofmann, V. A. de La Peña O'Shea, F. E. Oropeza, *J. Mater. Chem. A* **2021**, *9*, 19465.
[54] Y. Zhou, S. Sun, C. Wei, Y. Sun, P. Xi, Z. Feng, Z. J. Xu, *Adv. Mater.* **2019**, *31*, 1902509.
[55] B. Cui, H. Lin, J.-B. Li, X. Li, J. Yang, J. Tao, *Adv. Funct. Mater.* **2008**, *18*, 1440.
[56] J. Kubisztal, M. Kubisztal, *Catalysts* **2022**, *12*, 21.
[57] C. Simon, J. Timm, D. Tetzlaff, J. Jungmann, U.-P. Apfel, R. Marschall, *ChemElectroChem* **2021**, *8*, 227.
[58] M. Li, Y. Xiong, X. Liu, X. Bo, Y. Zhang, C. Han, L. Guo, *Nanoscale* **2015**, *7*, 8920.
[59] K. Chakrapani, G. Bendt, H. Hajiyani, I. Schwarzrock, T. Lunkenbein, S. Salamon, J. Landers, H. Wende, R. Schlögl, R. Pentcheva, M. Behrens, S. Schulz, *ChemCatChem* **2017**, *9*, 2988.
[60] E. Rios, J.-L. Gautier, G. Poillerat, P. Chartier, *Electrochim. Acta* **1998**, *44*, 1491.
[61] H. Zhu, S. Zhang, Y.-X. Huang, L. Wu, S. Sun, *Nano Lett.* **2013**, *13*, 2947.
[62] J. R. Kitchin, J. K. Nørskov, M. A. Barteau, J. G. Chen, *Phys. Rev. Lett.* **2004**, *93*, 156801.
[63] I. E. L. Stephens, A. S. Bondarenko, F. J. Perez-Alonso, F. Calle-Vallejo, L. Bech, T. P. Johansson, A. K. Jepsen, R. Frydendal, B. P. Knudsen, J. Rossmeisl, I. Chorkendorff, *J. Am. Chem. Soc.* **2011**, *133*, 5485.
[64] F. Calle-Vallejo, M. T. M. Koper, A. S. Bandarenka, *Chem. Soc. Rev.* **2013**, *42*, 5210.
[65] J. O. Bockris, T. Otagawa, *J. Electrochem. Soc.* **1984**, *131*, 290.

[66] D. Stenzel, B. Zhou, C. Okafor, M. V. Kante, L. Lin, G. Melinte, T. Bergfeldt, M. Botros, H. Hahn, B. Breitung, S. Schweidler, *Front. Energy Res.* **2022**, *10*.
[67] P. Edalati, Q. Wang, H. Razavi-Khosroshahi, M. Fuji, T. Ishihara, K. Edalati, *J. Mater. Chem. A* **2020**, *8*, 3814.
[68] S. Nundy, D. Tatar, J. Kojčinović, H. Ullah, A. Ghosh, T. K. Mallick, R. Meinusch, B. M. Smarsly, A. A. Tahir, I. Djerdj, *Adv. Sustainable Syst.* **2022**.
[69] L. Tian, Z. Zhang, S. Liu, G. Li, X. Gao, *Energy Environ. Mater.* **2022**, *5*, 645.
[70] J. Ma, B. Zhao, H. Xiang, F.-Z. Dai, Y. Liu, R. Zhang, Y. Zhou, *J. Adv. Ceram.* **2022**, *11*, 754.
[71] A. Radoń, Ł. Hawełek, D. Łukowiec, J. Kubacki, P. Włodarczyk, *Sci. Rep.* **2019**, *9*, 20078.
[72] Y. Sharma, A. R. Mazza, B. L. Musico, E. Skoropata, R. Nepal, R. Jin, A. V. Ievlev, L. Collins, Z. Gai, A. Chen, M. Brahlek, V. Keppens, T. Z. Ward, *ACS Appl. Mater. Interfaces* **2021**, *13*, 17971.
[73] Y. Zhang, T. Lu, Y. Ye, W. Dai, Y. Zhu, Y. Pan, *ACS Appl. Mater. Interfaces* **2020**, *12*, 32548.
[74] K. Brezesinski, R. Ostermann, P. Hartmann, J. Perlich, T. Brezesinski, *Chem. Mater.* **2010**, *22*, 3079.
[75] T. Brezesinski, B. Smarsly, K. Iimura, D. Grosso, C. Boissière, H. Amenitsch, M. Antonietti, C. Sanchez, *Small* **2005**, *1*, 889.
[76] B. Smarsly, S. Polarz, M. Antonietti, *J. Phys. Chem. B* **2001**, *105*, 10473.
[77] P. Hartmann, D.-K. Lee, B. M. Smarsly, J. Janek, *ACS Nano* **2010**, *4*, 3147.
[78] L. A. Dubraja, C. Reitz, L. Velasco, R. Witte, R. Kruk, H. Hahn, T. Brezesinski, *ACS Appl. Nano Mater.* **2018**, *1*, 65.
[79] G. Wang, J. Qin, Y. Feng, B. Feng, S. Yang, Z. Wang, Y. Zhao, J. Wei, *ACS Appl. Mater. Interfaces* **2020**, *12*, 45155.
[80] P. Cop, S. Kitano, K. Niinuma, B. M. Smarsly, H. Kozuka, *Nanoscale* **2018**, *10*, 7002.
[81] B. S. Murty, J.-W. Yeh, S. Ranganathan, P. P. Bhattacharjee, in *High-Entropy Alloys*, Elsevier, Amsterdam, Netherlands**2019**.
[82] M. C. Gao, J.-W. Yeh, P. K. Liaw, Y. Zhang, *High-Entropy Alloys: Fundamentals and Applications*, Springer International Publishing, Cham **2016**.
[83] T. X. Nguyen, J. Patra, J.-K. Chang, J.-M. Ting, *J. Mater. Chem. A* **2020**, *8*, 18963.
[84] K. Brezesinski, J. Wang, J. Haetge, C. Reitz, S. O. Steinmueller, S. H. Tolbert, B. M. Smarsly, B. Dunn, T. Brezesinski, *J. Am. Chem. Soc.* **2010**, *132*, 6982.
[85] V. D'Ippolito, G. B. Andreozzi, D. Bersani, P. P. Lottici, *J. Raman Spectrosc.* **2015**, *46*, 1255.
[86] Z. Wang, D. Schiferl, Y. Zhao, H. S. C. O'Neill, *J. Phys. Chem. Solids* **2003**, *64*, 2517.
[87] A. C. Ulpe, K. C. Bauerfeind, L. I. Granone, A. Arimi, L. Megatif, R. Dillert, S. Warfsmann, D. H. Taffa, M. Wark, D. W. Bahnemann, *Z. Phys. Chem.* **2020**, *234*, 719.
[88] M. Einert, R. Ostermann, T. Weller, S. Zellmer, G. Garnweitner, B. M. Smarsly, R. Marschall, *J. Mater. Chem. A* **2016**, *4*, 18444.
[89] E. M. Mills, M. Kleine-Boymann, J. Janek, H. Yang, N. D. Browning, Y. Takamura, S. Kim, *Phys. Chem. Chem. Phys.* **2016**, *18*, 10486.
[90] C.-Y. Chiu, A. S. Chiang, K.-J. Chao, *Microporous Mesoporous Mater.* **2006**, *91*, 244.
[91] A. N. Mansour, R. A. Brizzolara, *Surf. Sci. Spectra* **1996**, *4*, 351.
[92] Y. K. Penke, G. Anantharaman, J. Ramkumar, K. K. Kar, *ACS Appl. Mater. Interfaces* **2017**, *9*, 11587.
[93] T. Saravanakumar, S. Sathiya Bama, T. Selvaraju, S. J. Sardhar Basha, *Energy Fuels* **2021**, *35*, 5372.
[94] Y.-T. Lu, Y.-J. Chien, C.-F. Liu, T.-H. You, C.-C. Hu, *J. Mater. Chem. A* **2017**, *5*, 21016.
[95] D. Wang, Z. Liu, S. Du, Y. Zhang, H. Li, Z. Xiao, W. Chen, R. Chen, Y. Wang, Y. Zou, S. Wang, *J. Mater. Chem. A* **2019**, *7*, 24211.
[96] P. van Attekum, J. M. Trooster, *J. Electron Spectrosc. Relat. Phenom.* **1980**, *18*, 135.
[97] R. P. Vasquez, *Surf. Sci. Spectra* **1993**, *2*, 13.
[98] R. D. Shannon, *Acta Crystallogr. A Cryst. Phys. Diffr. Theor. Gen. Crystallogr.* **1976**, *32*, 751.
[99] M. Einert, C. Wessel, F. Badaczewski, T. Leichtweiß, C. Eufinger, J. Janek, J. Yuan, M. Antonietti, B. M. Smarsly, *Macromol. Chem. Phys.* **2015**, *216*, 1930.
[100] H. Radinger, P. Connor, S. Tengeler, R. W. Stark, W. Jaegermann, B. Kaiser, *Chem. Mater.* **2021**, *33*, 8259.
[101] S. Peng, F. Gong, L. Li, D. Yu, D. Ji, T. Zhang, Z. Hu, Z. Zhang, S. Chou, Y. Du, S. Ramakrishna, *J. Am. Chem. Soc.* **2018**, *140*, 13644.
[102] J. Li, D. Chu, H. Dong, D. R. Baker, R. Jiang, *J Am Chem Soc* **2020**, *142*, 50.
[103] H. Keppler, *Phys. Chem. Miner.* **1996**, *23*, 288.
[104] M. R. Hoffman, S. T. Martin, W. Choi, D. W. Bahnemann, *Chem. Rev.* **1995**, *95*, 69.
[105] J. Krüger, R. Plass, M. Grätzel, P. J. Cameron, L. M. Peter, *J. Phys. Chem. B* **2003**, *107*, 7536.
[106] Y. Liu, F. L. Formal, F. Boudoire, N. Guijarro, *ACS Appl. Energy Mater.* **2019**, *2*, 6825.
[107] Y. Liu, F. L. Formal, F. Boudoire, L. Yao, K. Sivula, N. Guijarro, *J. Mater. Chem. A* **2019**, *7*, 1669.
[108] M. Barroso, S. R. Pendlebury, A. J. Cowan, J. R. Durrant, *Chem. Sci.* **2013**, *4*, 2724.
[109] A. J. Bard, A. B. Bocarsly, F. R. F. Fan, E. G. Walton, M. S. Wrighton, *J. Am. Chem. Soc.* **1980**, *102*, 3671.
[110] Y. Ma, Y. Hu, Y. Pramudya, T. Diemant, Q. Wang, D. Goonetilleke, Y. Tang, B. Zhou, H. Hahn, W. Wenzel, M. Fichtner, Y. Ma, B. Breitung, T. Brezesinski, *Adv. Funct. Mater.* **2022**, *32*, 2202372.
[111] R. van de Krol, M. Grätzel, in *Photoelectrochemical Hydrogen Production*, Springer, New York **2012**.
[112] B. S. Holinsworth, D. Mazumdar, H. Sims, Q.-C. Sun, M. K. Yurtisigi, S. K. Sarker, A. Gupta, W. H. Butler, J. L. Musfeldt, *Appl. Phys. Lett.* **2013**, *103*, 082406.
[113] C. Li, P. Li, L. Li, D. Wang, X. Gao, X. J. Gao, *RSC Adv.* **2021**, *11*, 21851.
[114] R. Zhang, Q. Yuan, R. Ma, X. Liu, C. Gao, M. Liu, C.-L. Jia, H. Wang, *RSC Adv.* **2017**, *7*, 21926.
[115] Y. Yang, S. Wang, C. Jiang, Q. Lu, Z. Tang, X. Wang, *Chem. Mater.* **2016**, *28*, 2417.
[116] M. P. Browne, H. Nolan, G. S. Duesberg, P. E. Colavita, M. E. G. Lyons, *ACS Catal.* **2016**, *6*, 2408.
[117] M. W. Kanan, D. G. Nocera, *Science* **2008**, *321*, 1072.
[118] N. Fairley, V. Fernandez, M. Richard-Plouet, C. Guillot-Deudon, J. Walton, E. Smith, D. Flahaut, M. Greiner, M. Biesinger, S. Tougaard, *Appl. Surface Sci. Adv.* **2021**, *5*, 100112.
[119] G. Kresse, J. Furthmüller, *Phys. Rev. B* **1996**, *54*, 11169.
[120] G. Kresse, D. Joubert, *Phys. Rev. B* **1999**, *59*, 1758.
[121] D. Gehringer, sqsgen, https://github.com/dgehringer/sqsgenerator (accessed: December 2022).
[122] C. C. L. McCrory, S. Jung, J. C. Peters, T. F. Jaramillo, *J. Am. Chem. Soc.* **2013**, *135*, 16977.